Journal of Alloys and Compounds 1058 (2026) 186976

Contents lists available at ScienceDirect

Journal of Alloys and Compounds

journal homepage: www.elsevier.com/locate/jalcom

First-principle DFT-based study of novel K_3SeI anti-perovskite for advanced photovoltaic and photocatalytic applications with SCAPS-1D solar cell modeling

Md. Earshad Ali [a,*], Karim Kriaa [b], Md. Nobiul Islam [a], Chemseddine Maatki [b], Md. Shizer Rahman [a], Noureddine Elboughdiri [c], Md. Azizur Rahman [d,**]

[a] Department of Electrical and Electronic Engineering, Jamalpur Science & Technology University, Jamalpur 2012, Bangladesh
[b] College of Engineering, Imam Mohammad Ibn Saud Islamic University (IMSIU), Riyadh 11432, Saudi Arabia
[c] Chemical Engineering Department, College of Engineering, University of Ha'il, P.O. Box 2440, Ha'il 81441, Saudi Arabia
[d] Department of Electrical and electronic Engineering, Begum Rokeya University Rangpur, Rangpur 5404, Bangladesh

ARTICLE INFO

Keywords:
K_3SeI anti-perovskite
Wide bandgap
Optoelectronic Material
Photocatalysis
Energy material
Photovoltaic

ABSTRACT

Anti-perovskite compounds have recently become a focus of particular interest as potential components for lead-free, environmentally friendly, and low-cost renewable energy technologies. Their structural stability, tunable electronic properties, and excellent optical capabilities have led to their increasingly widespread use in photovoltaic, optoelectronic, and photocatalytic applications. In this study, the structural, mechanical, optoelectronic, dynamic, defect, surface, photovoltaic, and photocatalytic properties of the K_3SeI anti-perovskite compound have been systematically analyzed, using DFT-based GGA–PBE functionals. Structure optimization, phonon, and elastic constants analysis confirmed that K_3SeI is structurally, dynamically, and mechanically stable. The material exhibits a direct bandgap of 1.7047 eV (PBE) and 2.5367 eV (HSE06) at the Γ–Γ point, which is highly suitable for solar cells, and visible light-dependent water splitting. Optical properties show that K_3SeI exhibits a strong absorption coefficient ($\alpha \approx (6.8–0.5)\times 10^5$ cm^{-1}) in the ultraviolet to visible wavelength. Analysis of the $2 \times 2 \times 1$ K_3SeI supercell shows that vacancy formation is easiest in iodine, while potassium and selenium are relatively stable, which provides important guidance for defect management and material optimization. The (001) surface of K_3SeI anti-perovskite is thermodynamically very stable, with a surface energy of only 0.000514 eV/$Å^2$. Adsorption studies demonstrate that OH* and OOH* intermediates are more tightly bound than H* and O*, ensuring the stability of the important reaction species. The overpotential of the hydrogen evolution reaction (HER) is only 0.071 V, demonstrating the catalytic efficiency of the surface, while the overpotential of the oxygen evolution reaction (OER) is relatively high (2.64 V). Also, the photovoltaic performance was tested by modeling the Al/FTO/SnS_2/K_3SeI/CuO/Se solar cell structure in SCAPS-1D. After optimization, the highest results were obtained with J_{SC} of 31.71 mA/cm^2, V_o of 1.1355 V, FF of 82.88 %, and PCE of 29.84 %. These results were obtained when the defect density was 10^{15} cm^{-3}, the shallow acceptor concentration was 10^{15} cm^{-3}, and the series–shunt resistance was 1.48 Ω.cm^2 and 10^6 Ω.cm^2, respectively. Overall results indicate that K_3SeI is a highly promising, environmentally friendly, lead-free, and high-efficiency material, which is particularly suitable for next-generation photovoltaic devices, visible light-dependent water splitting technologies, and advanced optoelectronic devices.

1. Introduction

In the current world, the energy crisis, the increasing demand for semiconductor materials for optoelectronic technology, and environmental problems have further increased the importance of discovering sustainable and renewable energy sources. The development of new materials with improved properties for next-generation electronic and electrical devices is now one of the main aims of

---

* Corresponding author.
** Corresponding Author

E-mail addresses: md.earshadali28@gmail.com (Md.E. Ali), azizurrahmanatik49@gmail.com (Md.A. Rahman).

https://doi.org/10.1016/j.jallcom.2026.186976
Received 24 November 2025; Received in revised form 25 January 2026; Accepted 21 February 2026

modern scientific research [1,2]. In this context, the main objective of this research is to make renewable energy production more efficient. In recent years, perovskite materials have revolutionized photocatalysis and photovoltaic technologies [3–5]. In particular, the use of these materials has significantly increased the overall performance of the devices involved [6]. The efficiency of perovskite solar cells (PSCs) increased from 3.8 % to 26.7 % between 2009 and 2024, further strengthening the potential of this material class [6–9]. Additionally, in 2019, researchers experimentally achieved solar-to-hydrogen conversion efficiencies of up to 17 % in a $MAP(I_{0.85}Br_{0.15})_3/Si$ structure [10], reflecting the extraordinary potential of perovskite materials in renewable energy technologies.

Currently, there are still some serious challenges in the industrialization process of perovskite material-based solar cells and photocatalysis. Chief among these are the device stability, long-term light and air degradation, and the toxicity of the materials used. Considering these issues, anti-perovskite structure materials have gained special attention in recent research [5,11,12]. Anti-perovskite is a new type of perovskite structure in which the conventional ABX_3 perovskite structure is reversed and arranged in the X_3BA form. Here X is a positive ion (A^+), B is a divalent negative ion (B^{2-}) and A is a single negative ion (X^-) [13–15]. Such anti-perovskite materials are naturally occurring on Earth, non-toxic, and exhibit a bandgap suitable for solar cells [16–18]. Recent research has shown that anti-perovskite materials have potential in various fields of modern technology, for example, optoelectronic devices, solar energy harvesting, X-ray and radiation detection, light detection (infrared, UV, and visible), UV protection, data storage, sensors, superconductors, hydrogen storage, optical fibers, and photocatalysis. Research has shown that these materials are highly suitable and effective for all these uses [4,5,11,12,19–23].

However, considering the various limitations of perovskite materials in the present study, the main goal of this research was to explore new materials that are non-toxic in nature, environmentally friendly, and appropriate for use in photocatalysis and solar cells. It is possible to evaluate the efficiency of photovoltaic conversion with such materials. With this goal in mind, this study has designed the K_3SeI anti-perovskite compound. It is lead-free, less harmful to human health, and environmentally friendly, and it contains relatively safe ingredients, such as potassium, selenium, and iodine. Typically, such anti-perovskite compounds crystallize in a cubic structure and exhibit $Pm\bar{3}m$ space group symmetry, which is shown in Fig. 1(a). Recently, the water splitting process of Co_3ZnN-based anti-perovskite Co_3ZnN/C structure was extensively studied [22]. On the other hand, hydride compounds, such as K_3SH, K_3SeH and K_3TeH, exhibit hydrogen contents of 3.24, 2.49 and 2.008 wt%, respectively, which are liberated at temperatures of 963.88, 793.19 and 672.70 K, respectively; as a result, these compounds show significant potential for hydrogen storage [23]. Thin-film all-solid-state batteries (ASSB) were prepared using a layer-by-layer technology with $LiCoO_2/Li_3OCl$/graphite composition, and they possessed an initial discharge capacity of 120 mAh g^{-1} in the voltage range of 2.2–4.2 V [24,25]. Recent studies have shown that the hydrogen production rate of anti-perovskite Co_3ZnN under visible light is about six times higher, which is evidence of its high photocatalytic efficiency [26]. Furthermore, theoretical analysis has shown that it is possible to significantly enhance the hydrogen generation efficiency (HER) of anti-perovskite Ni_3InN through strain control and doping [27]. Recent studies of X_6BiSbN_2 (X = Mg, Ca, Sr) double anti-perovskites have demonstrated that Ca_6BiSbN_2 and Sr_6BiSbN_2 are suitable for the absorber layer of anti-perovskite cells, X_6BiSbN_2 (X = Mg, Ca, Sr) is useful as a potential photodetector material, and Sr_6BiSbN_2 is suitable for thermoelectric applications [28]. In 2025, studies on Ni_3AC (where A = Mg, Zn, Cd) anti-perovskites showed that Ni_3MgC acts as a superconductor and has a transition temperature (T_C) of 8.644 K [29]. In 2024, p-type doping of Sr_3BiN and Mg_3BiN achieved maximum thermoelectric figure of merit (ZT) of 1.49 and 1.18 at 900 K, respectively, making them suitable for thermoelectric applications [30].

This study presents a new lead-free K_3SeI anti-perovskite compound, and its structural, mechanical, electrostatic potential, dynamic, optoelectronic, vacancy defect, surface, photovoltaic, and photocatalysis features are analyzed using DFT-based methods. The phonon band structure and elastic constants of the compound indicate that it is mechanically and dynamic stable, making K_3SeI optimal for advanced technological applications. This compound exhibits a direct bandgap of 1.7047 eV (PBE) and 2.5367 eV (HSE06) at the Γ-point, which is ideal for absorption of visible light. In addition, it exhibits high optical absorption in the range of 6.8×10^5–0.5×10^5 cm^{-1} from ultraviolet to visible light wavelengths, which is very critical for photocatalysis and solar cells. Analysis of the 2 × 2 × 1 K_3SeI supercell reveals that iodine atoms are more prone to vacancy formation, whereas potassium and selenium remain relatively stable, offering important guidance for defect management and material optimization. Also, the (001) surface of K_3SeI anti-perovskite is very thermodynamically stable, with a surface energy of only 0.000514 eV/$Å^2$. Adsorption analysis shows that OH* and OOH* intermediates are more tightly bound than H* and O*,

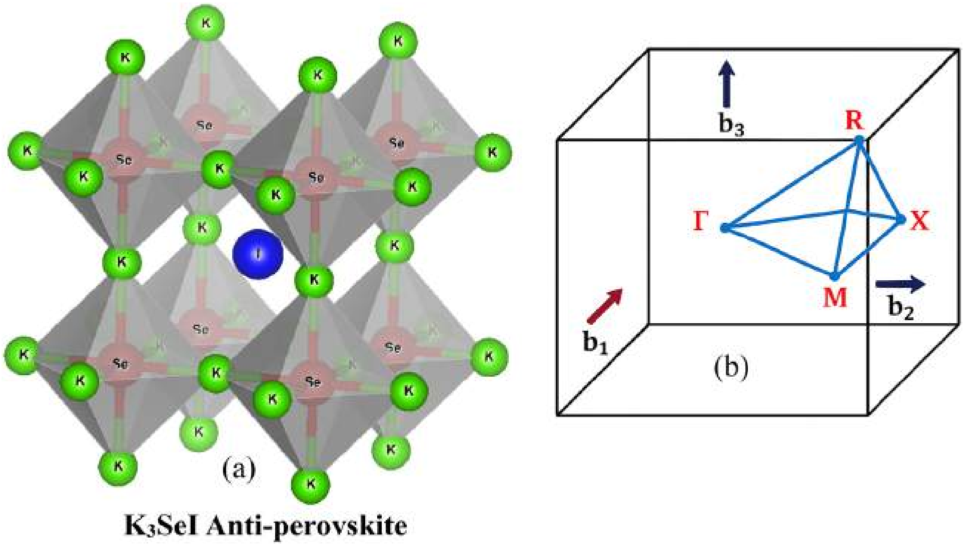

Fig. 1. (a) Optimized cubic crystal structure of the K_3SeI anti-perovskite, and (b) the corresponding Brillouin zone with selected k-path used for calculating the electronic band structure.

ensuring the stability of the important reaction species. The overpotential for the hydrogen evolution reaction (HER) is only 0.071 V, which demonstrates the catalytic efficiency of the surface, while the overpotential for the oxygen evolution reaction (OER) is relatively high (2.64 V). The Al/FTO/SnS_2/K_3SeI/CuO/Se device exhibits good charge generation and low recombination, which is supported by favorable band alignment and efficient carrier transport. The PV performance is remarkable, with $J_{SC} = 31.71$ mA/cm^2, $V_o = 1.1355$ V, FF = 82.88 %, and PCE = 29.84 %, while the moderate defect density (10^{15} cm^{-3}), shallow acceptor concentration (10^{15} cm^{-3}), and series-shunt resistance (1.48 and 10^6 Ω.cm^2) further enhance efficiency and stability. Overall, the result demonstrates the visible light-dependent photovoltaic performance of the K_3SeI compound and its potential for solar-based hydrogen production. From an environmental perspective, the features of the K_3SeI compound indicate that it can be effectively utilized not only for water splitting but also in various sustainable energy conversion processes.

2. Simulation methodology

2.1. DFT-based first-principles computational approach to the 3D bulk cubic crystal structure of K_3SeI anti-perovskite

In this study, the structural, electrical, optical, dynamic, and mechanical features of the designed compound K_3SeI were analyzed using first-order Density Functional Theory (DFT) methods [31–33]. The calculations were performed using Quantum ESPRESSO software, which is known as an efficient and reliable platform for determining various electronic structures and material-related properties [1,2,43]. The scalar-relativistic Norm-Conserving (NC) pseudopotentials have been applied for structural optimization, electronic structure, mechanical stability, and phonon-based analysis [34][35]. The analysis of the effect on the total energy in the conducted plane-wave-based calculations (shown in Fig. 2(a)) indicates that the energy converges appropriately at ecutwfc = 40 Ry and ecutrho = 240 Ry. However, for more accurate results, ecutwfc = 60 Ry and ecutrho = 360 Ry were used in all final calculations [36][37]. Therefore, to verify the sampling of the Brillouin zone, Γ-centered Monkhorst–Pack k-point grids ranging from 1 × 1 × 1–8 × 8 × 8 have been tested, as shown in Fig. 2(b). Although the energy value remains stable on a 4 × 4 × 4 grid (as shown in Fig. 2 (b)), a 6 × 6 × 6 Γ-centered k-point grid was adopted in all calculations for more reliable results. A strong convergence threshold of 1×10^{-6} Ry has been determined to maintain high accuracy in electronic self-consistent field (SCF) calculations [38]. All these convergence tests confirm that the computational setup used makes the research results reliable and numerically stable. However, for a more accurate prediction of the bandgap, the HSE06 hybrid functional has been used. In this case, a 6 × 6 × 6 Γ-centered k-point grid and a 6 × 6 × 6 q-point mesh of equal density are adopted for Brillouin zone sampling, which ensures the accuracy of the hybrid functional calculations. Additionally, the norm-conserving pseudopotential has been used, which is particularly useful in correctly considering unoccupied electronic states in determining optical properties [39]. In more detail, an 8 × 8 × 8 Γ-centered k-point grid has been used in the analysis of optical absorption, dielectric function, and associated electronic transitions [40–43]. To analyze the vacancy defect formation energy of K_3SeI anti-perovskite, a 2 × 2 × 1 supercell was constructed, with lattice parameters a = b = 12.4733 Å and c = 6.2365 Å. For Supercell's DFT-based

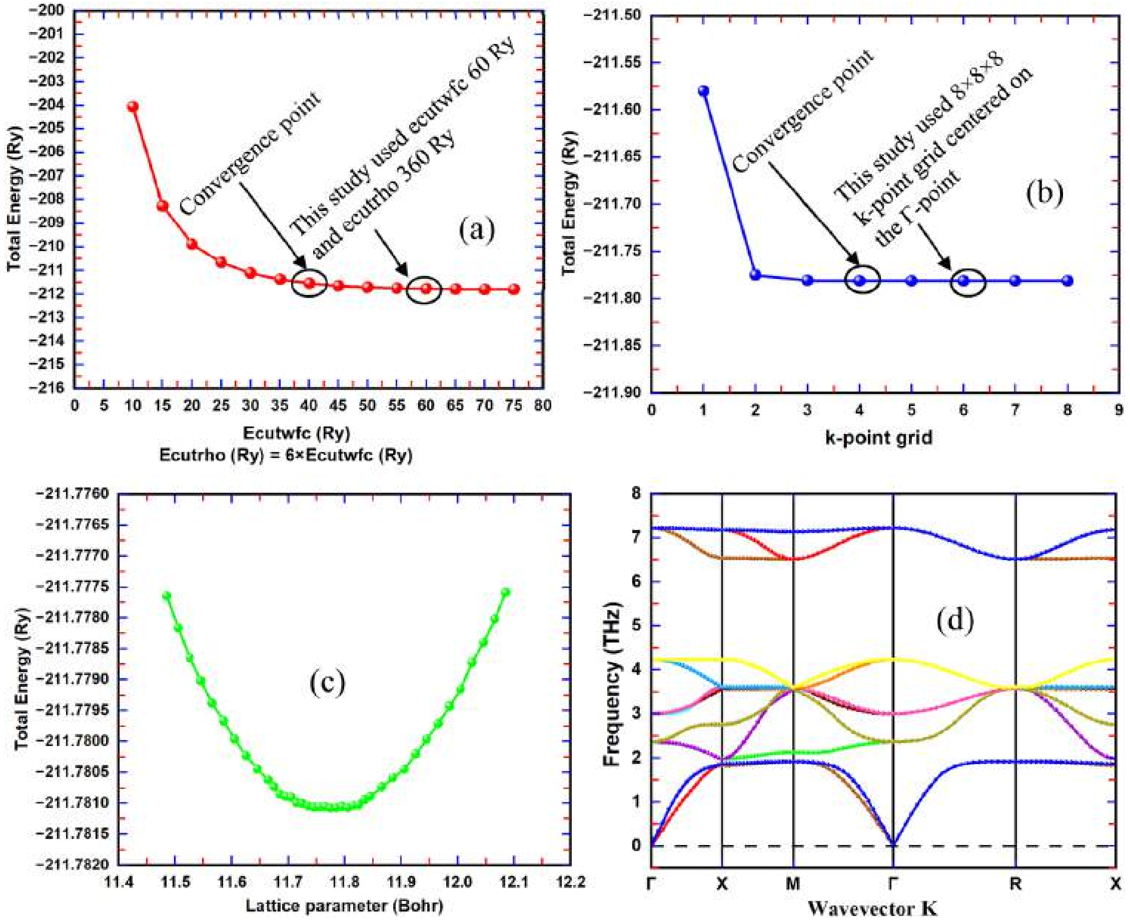

Fig. 2. (a) Optimized ecutrho and ecutwfc, (b) Optimized K-mesh, (c) Optimized lattice parameter and (b) phonon dispersion characteristics of the K_3SeI anti-perovskite.

first-principles calculations, a plane-wave cut-off energy ecutwfc of 40 Ry and a charge density cut-off ecutrho of 240 Ry are used. A $3 \times 3 \times 3$ Monkhorst–Pack k-point mesh was selected for Brillouin zone sampling, and the Gamma point-centered scheme was applied. The positions of all atoms are completely relaxed, with the force convergence threshold kept at 1×10^{-4} Ry and the total energy convergence at 1×10^{-4} Ry. Energy convergence up to 1×10^{-6} Ry has been confirmed for self-consistent field (SCF) calculations. Using this setup, the vacancy defect formation energy of single K, Se, and I atoms has been determined, which provides important information in analyzing the defect behavior and stability of the material [44–48].

2.2. *DFT-based first-principles computational approach to the (001) surface of K_3SeI anti-perovskite*

In addition, the electrostatic potential of the compound was determined. The three-dimensional bulk structures, there is no definite surface or boundary, so a slab with a vacuum layer is required to accurately analyze the potential profile. For this purpose, the bulk K_3SeI structure was first transformed into a (1 1 2) supercell, and then a slab was prepared along the (0 0 1) direction. The lattice parameters of the slab are taken as a = b = 6.2365 Å, and a vacuum of c = 25 Å is kept along the z-direction to avoid slab–slab interaction. A total of 6 at. layers are used, with KI termination at the top and K_2Se termination at the bottom. The bottom 3 at. layers of the slab are fixed in the bulk position, and the top 3 layers are completely relaxed. Structural relaxation is performed using a force threshold of 1×10^{-4} Ry and a total energy convergence value of 1×10^{-4} Ry. An accuracy value of 1×10^{-6} Ry has been set for electronic self-consistent field (SCF) calculations so that the results are sufficiently reliable and numerically stable. For the plane-wave based DFT calculations, the kinetic energy cutoff was ecutwfc = 40 Ry and the charge density cutoff was ecutrho = 240 Ry. For Brillouin zone sampling, a Γ-centered $4 \times 4 \times 1$ Monkhorst–Pack k-point mesh was adopted in the slab model, where the k-point shift was (0 0 0) [49–52]. The surface energy, adsorption energy, free energy diagram, and overpotential voltage of the (001) surface were determined using the same slab model used for electrostatic potential analysis. In this case, the lattice parameters of the slab are set to a = b = 6.2365 Å, and the thickness of the vacuum layer along the z-direction is increased to c = 30 Å so that slab-slab interaction can be completely avoided. Structural relaxation was performed using the same computational parameters. The adsorption energy was determined by adding different adsorbates (H*, O*, OH*, OOH*) to this optimized slab model. The surface energy was calculated using the difference between the bulk and slab energies. The corresponding overpotential was determined by constructing free energy diagrams to analyze the efficiency of HER and OER reactions. The optimized slab structure with adsorbates (H*, O*, OH*, OOH*), which is shown in Fig. 3(a), Fig. 3(b), Fig. 3(c), and Fig. 3 (d). The adsorption energy was determined by adding different adsorbates (H*, O*, OH*, OOH*) to this optimized slab model [53–58]. The surface energy was calculated using the difference between the bulk and slab energies. In order to calculate the adsorption energies of H*, O*, OH*, and OOH* on the (001) surface of K_3SeI, reference energies of gas-phase species were determined using the same DFT parameters. For H_2, O_2, and H_2O molecules, cubic simulation boxes of sizes a = b = c = 15.5 Å, 17 Å, and 23 Å, respectively, were used to avoid interaction between periodic images. All gas-phase molecules were fully relaxed under the same computational settings to obtain accurate total energies. These reference energies were then employed in the adsorption energy calculations to ensure consistency and reliability in evaluating the interaction of adsorbates with the slab surface. The corresponding overpotential was determined by constructing free energy diagrams to analyze the efficiency of HER and OER reactions. In constructing the free energy diagram, values from previously published literature were used to correct ΔZPE (zero-point energy) and TΔS (entropy), which made the thermodynamic analysis of HER and OER reactions more realistic [53–56].

2.3. *The computational technique of the solar cell device design and simulation for K_3SeI anti-perovskite*

SCAPS-1D (version 3.3.09) software was used to analyze the solar cell performance of the proposed inorganic anti-perovskite material K_3SeI in this study. Developed by Professor Marc Borgelman of Ghent University in Belgium, this software is widely used in the research community because it can reliably analyze the performance of semiconductor solar cells with different layers [59–61]. SCAPS-1D is compatible with other device simulation platforms and also facilitates comparison with reported results from previous studies, making it more suitable for this work. In this study, a solar cell structure was first constructed on SCAPS-1D, with the layering: Al/FTO/SnS_2/K_3SeI/CuO/Au. Here, Al is used as a front contact with a work function of 4.1 eV [62] and Se is used as a back contact with a work function of 5.9 eV [59] to effectively collect the generated photocarriers. All simulations were performed at a temperature of 300 K, AM_1.5 G standard solar irradiance (1 sun), and a frequency of 1.0×10^6 Hz, which closely mimics the operation of solar cells in real environments. Additionally, the defect density, shallow acceptor density, electron mobility, hole mobility, and the effects of series and shunt resistance are all optimized to achieve the best photovoltaic performance. SCAPS-1D can create devices with up to

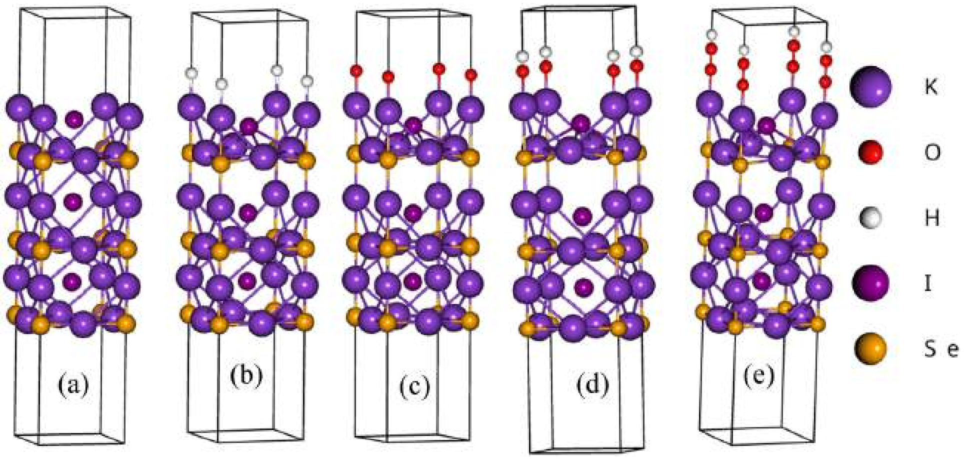

Fig. 3. Optimized structure (a) (001) surface, (b) (001) surface+H, (c) (001) surface+O, (d) (001) surface+OH, and (e) (001) surface+OOH of the K_3SeI anti-perovskite.

seven layers, and the layers can be defined as n-type, p-type, or intrinsic. The fundamental basis for determining the physical behavior of the device is three simultaneous differential equations: the continuity equation, the transport equation, and the Poisson equation. Together, these equations accurately describe the charge transport, carrier generation–recombination, and electric field distribution of semiconductor devices. As a result, the photovoltaic performance of solar cells, such as J–V characteristics, quantum efficiency, open circuit voltage, fill factor, and conversion efficiency, can be reliably determined [59–63].

3. Result and discussion

3.1. Structural characteristics of the K_3SeI anti-perovskite

Cubic crystal structure of the K_3SeI compound, which belongs to the Pm3¯m space group, is shown in Fig. 1(a). In this structure, a maximum of five atoms can be placed in a unit cell. The K cations are located at coordinates (0.5, 0, 0), (0, 0.5, 0) and (0, 0, 0.5), and they are in octahedral coordination. The Se atoms are located at face-centered positions (0, 0, 0). On the other hand, the I ions are located at coordinates (0.5, 0.5, 0.5) and fill halogen positions at the center of the unit cell. In Fig. 1 (b) is the Brillouin zone of a cubic crystal, which is very important for band structure analysis. In this study, the Γ–X–M–Γ–R–X path is used to determine the band structure. Fig. 2(c) shows how the total energy (E_o) varies with changes in lattice parameters. In general, the lower the energy, the more stable is the structure. Stability analysis (convergence test) was conducted by varying various cell parameters and k-point grid to ensure structural accuracy. In Table 1 are the optimal cell parameter (a_o), unit cell volume (V_o), and total energy (E_o) obtained in this study and the values reported for related crystals in previous studies. A 60 Ry kinetic energy cut-off, a 360 Ry charge density cut-off, and an 6 × 6 × 6 k-point grid were used for this structural optimization.

3.2. Phonon dispersion behavior of K_3SeI anti-perovskite

The natural vibrations of atoms in a crystal structure and the energy interaction between them are commonly called phonon scattering [67,68]. Phonon scattering is an important process that affects the thermal properties, energy transport, and kinetic behavior of materials. On the other hand, the analysis of phonon dispersion and lattice vibrations is very helpful in understanding the dynamic stability, vibrational properties, and thermal response of materials [69–71]. This ensures how stable and reliable the material is in various physical and technical applications. Phonon calculations of the K_3SeI compound were completed after appropriate optimizing its atomic arrangement and cell parameters [72–74]. The phonon band structure is analyzed in the initial part of the Brillouin zone, especially along the Γ–X–M–Γ–R–X path (Fig. 2(d)). This specific path dictates the phonon's kinetic energy distribution and energy divergence, which is important for understanding the different vibrational modes within the crystal structure. According to the analysis of the dispersion map given in Fig. 2(d), it can be seen that there is no negative or imaginary frequency in the phonon band of the K_3SeI compound. This clearly indicates that the compound is dynamically completely stable, i.e., there are no natural vibrational instabilities or frequency inversions in the crystal structure. This result confirms the physical durability of the material and shows that it will remain effective even in long-term use without any structural degradation. Consequently, this stability proves that the proposed K_3SeI anti-perovskite compound is quite suitable for use in photovoltaic, optoelectronic, and photocatalysis devices. As the vibrational stability and energy transport capability of the material are elucidated through phonon analysis, it provides a reliable basis for analyzing the electronic and optical features in the next step.

Table 1
Cell parameter, unit cell volume, and total energy of K_3SeI anti-perovskite in comparison with previously published data for validation.

Compound	a_0 (Å) (a = b = c)	Unit cell-volume V_o (a.u)^3	Total energy E_0 (Ry)	Reference
Na_3SI	5.321	1016.77	-345.7364	[1]
K_3SeI	6.2365	1637.024	-211.7811	This work
Na_3SBr	5.2576	980.80	-611.3479	[2]
Na_3OI	4.74	718.697	-5166.15	[64]
Na_3OBr	4.57	-	-	[65]
Na_3OCl	4.53	-	-	[66]
K_3OI	5.37	1045.029	-3614.13	[64]

3.3. Mechanical stability and elastic properties of K_3SeI anti-perovskite

Analyzing the elastic constant behaviour of a solid material is extremely important, as these properties directly affect the structural stability of the material, response to external forces, and performance in various technical applications [75,76]. In particular, elastic constant determination using the thermo_pw module of software such as Quantum ESPRESSO provides detailed information about the micro-level stiffness, ductility, and resistance to deformation of a material. Such information is crucial not only for fundamental physics but also for the development of photocatalysis, photovoltaics, and optoelectronic device. In this work, the calculation of elastic constants was carried out to determine the mechanical properties of K_3SeI anti-perovskite elements. The stiffness, decompression resistance, and deformation resistance of the material have been determined. The results obtained according to the used formulas and calculation methods are presented in Table 2 [77–86]. These results provide a clear idea of the mechanical stability of the material, its durable structure, and its ability to be used in technical applications. The results show that the structure of the K_3SeI compound exhibits high elastic modulus and stability, indicating that it is able to withstand changes in external pressure and force and is suitable for various device applications; for example, it can be used in photovoltaic cells, optoelectronic devices, and photocatalysis.

Mechanical stability criteria (Born criteria; cubic crystal): $C_{11} - C_{12} > 0$, $C_{11} + 2C_{12} > 0$, and $C_{44} > 0$ (1)

$$\text{Bulk modulus} : B = \frac{C_{11} + 2C_{12}}{3} \tag{2}$$

Table 2
Elastic and mechanical characteristics of K_3SeI anti-perovskite.

Mechanical/Elastic features	Mechanical/Elastic features value
Elastic constant C_{11}	26.768 GPa
Elastic constant C_{12}	0.892 GPa
Elastic constant C_{44}	3.252 GPa
$C_{11} - C_{12}$, $C_{11} + 2\,C_{12}$, and C_{44}	25.876, 28.552, and 3.252 (GPa) which > 0, Stable
Bulk modulus, B	9.517 GPa
Shear modulus for Voigt approximation, G_v	7.126 GPa
Shear modulus for Reuss approximation, G_R	4.643 GPa
Shear modulus For Voigt-Reuss-Hill average, G	5.885 GPa
Young’s modulus, E	14.63 GPa
Poission’s ratio, V	0.244
Pugh’s ratio, (B/G)	1.618
Cauchy pressure, $C_{12} - C_{44}$	–2.36 GPa
Zener anisotrop, A	0.251
Universal aniostropy index, A^U	2.675
Shear sound velocity, V_S	1627.5 ms^{-1}
Longitudinal sound velocity, V_L	2795.6 ms^{-1}
Average Debye sound velocity, V_m	1708.9 ms^{-1}
Debye temperature, Θ_D	139.7 K

$$\text{Shear modulus(G)}: \text{For Voigt approximation}: G_V = \frac{C_{11} - C_{12} + 3C_{44}}{5} \tag{3}$$

$$\text{For Reuss approximation}: \quad G_R = \frac{5(C_{11} - C_{12})C_{44}}{4C_{44} + 3(C_{11} - C_{12})} \tag{4}$$

$$\text{For Voigt} - \text{Reuss} - \text{Hill average}: G = \frac{G_V + G_R}{2} \tag{5}$$

$$\text{Young's modulus}: E = \frac{9BG}{3B + G} \tag{6}$$

$$\text{Poission's ratio}: V = \frac{3B - 2G}{2(3B + G)} \tag{7}$$

$$\text{Ductility Vs.Brittleness(Pugh's ratio)}: \frac{B}{G} > 1.75;\ \text{ductile and If}\ \frac{B}{G} < 1.75;\ \text{brittle} \tag{8}$$

Cauchy pressure (bound nature):

$C_{12} – C_{44} > 0$; metallic and $C_{12} – C_{44} < 0$; covalent/directional bonding tendency (9)

Elastic anisotropy:

$$\text{Zener anisotropy}: A = \frac{2C_{44}}{C_{11} - C_{12}} \text{and Universal aniostropy index}: A^U = 5\frac{G_V}{G_R} + \frac{B_V}{B_R} - 6 \tag{10}$$

$$\text{Soundvelocity\&Debyetemperature}: \text{Shearsoundvelocity}: \quad V_S = \sqrt{\frac{G}{\rho}} \tag{11}$$

$$\text{Longitudinal sound velocity}: \quad V_L = \sqrt{\frac{3B + 4G}{3\rho}} \tag{12}$$

$$\text{Average sound velocity}: \quad V_m = \left[\frac{1}{3}\left(\frac{2}{V_s^3} + \frac{1}{V_L^3}\right)\right]^{-\frac{1}{3}} \tag{13}$$

$$\text{Debye temperature}: \quad \Theta_D = \frac{h}{K_B}\left(\frac{3n}{4\pi V}\right)^{\frac{1}{3}} V_m \tag{14}$$

Here, h and K_B are the Planck and Boltzman constant, respectively, n is the atom number per unit cell, V is the unit cell volume, and ρ is the density [77–86].

Analysis of the mechanical characteristic of the K_3SeI compound provides critical insights into its bonding nature, stability, and potential device applications. According to the values in Table 2, the elastic constants of this compound are $C_{11} = 26.768$ GPa, $C_{12} = 0.892$ GPa, and $C_{44} = 3.252$ GPa, which fully satisfy the Born stability criteria ($C_{11}–C_{12} > 0$, $C_{11}+ 2\ C_{12} > 0$, $C_{44} > 0$). This confirms that K_3SeI is mechanically stable and less likely to undergo structural breakdown under external stress. The bulk modulus $B = 10.403$ GPa, shear modulus $G = 5.854$ GPa, and the Young modulus $E = 14.79$ GPa were obtained. The relatively low bulk modulus indicates that K_3SeI can be easily compressed, i.e., it is a relatively soft material. The values of the Pugh ratio ($B/G = 1.618$) and Poisson's ratio ($\nu = 0.244$) indicate that the compound is in the transitional zone between brittleness and near ductility. As a result, it has a reasonable ability to maintain a rigid structure even if it cannot withstand moderate mechanical loads. The negative value of the Cauchy pressure ($C_{12} – C_{44} = –2.36$ GPa) indicates that the material has a predominance of covalent bonds, which is highly beneficial for electron transport and dielectric properties. Although the crystal belongs to a cubic symmetry, the deviation of the Zener anisotropy factor ($A = 0.252$) from unity and the non-zero universal anisotropy index ($A^U = 2.675$) confirm the presence of elastic anisotropy, leading to different elastic responses along different crystallographic directions. The sound velocity analysis shows the shear sound velocity $V_S = 1627.5$ m/s and the longitudinal velocity $V_L = 2795.6$ m/s, with an average Debye velocity $V_m = 1708.09$ m/s. Also, the Debye temperature is about 139.7 K, indicating its thermal stability to be medium-level. Overall, the K_3SeI compound is a mechanically stable material with a clearly anisotropic nature and moderate thermal tolerance. Its covalent bonddependent brittle nature and good elastic response make it a potential material for applications, such as optical, electronic, and energy devices, where structural stability and efficient charge transport are both important [77–86].

3.4. Thermodynamic stability and formation energy analysis of K_3SeI anti-perovskite

Formation energy is a very important parameter in calculating the thermodynamic stability of a solid. It basically indicates how energetically stable the compound is compared to its constituent atoms or ideal ground state. In this study, the formation energy of the K_3SeI compound was determined using the total energy values obtained from first-principles (DFT) calculations, according to Eqs. (15) and (16) [87–90]. The corresponding results are shown in Table 3. According to calculations, the total formation energy of the K_3SeI compound was found to be −14.66 eV, and the formation energy per atom was found to be −2.86 eV/atom. Both values being negative indicate that the synthesis of the compound is energetically favorable and that it is capable of forming spontaneously. This provides evidence for the existence of strong chemical bonds between the K, Se, and I atoms, which makes the entire crystal structure thermodynamically stable. This stability provides an important basis for the usability and potential technological applications of the compound.

$$\text{Formation Energy}, \Delta E_f = E_{tot}^{K_3SeI} - \left(3E_{tot}^{K} + E_{tot}^{Se} + E_{tot}^{I}\right) \tag{15}$$

$$\text{Formation Energy per Atom}, \Delta E_f^{per\ atom} = \frac{E_{tot}^{K_3SeI} - \left(3E_{tot}^{K} + E_{tot}^{Se} + E_{tot}^{I}\right)}{5} \tag{16}$$

3.5. Electronic characteristics of the K_3SeI anti-perovskite

The energy levels of electrons in an object, their arrangement, and the nature of their motion play a key role in determining the electronic characteristic of that object. These properties determine how much electrical conductivity the material will exhibit and how it will respond to electric fields. Three important components are usually considered in the analysis of electronic behavior: band structure, electrostatic potential, and partial density of states (PDOS) [91–96]. Electrostatic potential analysis was particularly important in this study, as it can be used to determine electron affinity, which is considered an essential criterion in evaluating whether a element is optimal for use in solar cells or photocatalytic applications [22,23,73]. Analysis of the above properties was essential to understand whether the newly proposed structure of the

Table 3
Formation energy and total energy for K_3SeI anti-perovskite.

Material	Total energy (Ry)	Total energy (eV)	Atom number	Formation energy (eV)	Formation energy per atom (eV)
K_3SeI	−211.781	−2880.77	5	−14.66	−2.86
K	−56.435	−767.61	1	-	-
Se	−18.618	−253.16	1	-	-
I	− 22.843	−310.49	1	-	-

K_3SeI anti-perovskite compound could be used in practical electronic devices. The band structure, PDOS, and potential profile provide reliable information about its carrier transport, energy level configuration, and potential applications [91–93].

3.5.1. *Electronic bandgap behavior in K_3SeI anti-perovskite*

Fig. 4(a) shows the band structure of K_3SeI, where the Fermi level is taken as the zero energy point. From the analysis of the band structure, it is seen that both the VBM and the CBM are located at the Γ (gamma) point. This clearly shows that K_3SeI is a direct band-gap semiconductor, with a band gap of approximately 1.7047 eV (GGA-PBE) and 2.5367 eV (HSE06) [97–101]. Such direct band-gap semiconductor components are of great critical for their applicability in electronic, photovoltaic, optoelectronic, and photocatalytic devices. In particular, direct bandgap materials make it easier to create electron-hole pairs, which makes the process of energy conversion and light absorption more efficient. The value of the band gap plays a critical role not only in determining the optical performance of the device but also in the photocatalytic reaction and photovoltaic cell. For example, in the case of water splitting, a theoretically minimum band gap of 1.23 eV is necessary, which makes the process energetically feasible. However, in practical applications, additional energy or overpotential is necessary to generate hole-electron pairs. Therefore, it is ideal for the band gap to be somewhat higher for an effective photovoltaic and photocatalytic process. Studies have shown that the band gaps from 1.6 to 3.0 eV are mainly optimal for visible light absorption, which enhances photovoltaic and photocatalytic efficiency. On the other hand, if the band gap is greater than 3.1 eV, the material is not able to absorb visible light sufficiently, making the material inefficient in visible light-induced reactions [22,23,102,103].

In summary, the direct band gap and band gap value of K_3SeI make it a very promising candidate in electronic, photovoltaic, optoelectronic, and photocatalytic devices. This band structure analysis suggests that the electronic properties of the compound are suitable and that it enables efficient light absorption and energy conversion.

3.5.2. *Atomic orbital contributions in K_3SeI anti-perovskite*

Fig. 4(b) shows the PDOS of K_3SeI, where the contributions of different orbitals are marked in different colors. The horizontal axis indicates energy ($E–E_F$), where E_F is the Fermi level [90,91]. According to the distributions, the main contribution to the valence band comes from the Se_2p, K_3s, K_4p, K_5d, and I_2p orbitals, which are mainly concentrated in the energy range from −3 eV to −0.7047 eV. The density is particularly high between −2 eV and −0.7047 eV, which clearly indicates that selenium and iodine atoms are actively participating in the valence band formation. The contributions of other orbitals, such as K_1s, K_2p, Se_1s, Se_3d, I_1s, and I_3d are relatively limited. On the other hand, the conduction band is mainly formed in the energy range from 1 eV to 4.5 eV, where the K_3s, K_4p, K_5d, Se_3d, and I_3d orbitals make the main contributions. The contributions of the K_1s, K_2p, Se_1s, Se_2p and I_1s, I_2p, and orbitals are weak. Due to the absence of any states at the Fermi level, a specific band gap exists, which identifies the compound as a semiconductor. This PDOS analysis indicates that the electronic properties of the K_3SeI compound are well-structured and that it is a potential material for use in photovoltaic, optoelectronic, photocatalytic, and nano-devices [104,105].

3.5.3. *Effective mass and carrier mobility of K_3SeI anti-perovskite*

Analyzing the band gap structure of the K_3SeI compound, it was found that the value of electron and hole mobility in the band-edge region is important. From the bandgraph shown in Fig. 4(a) (GGA-PBE), the parabolic fitting method was used in the top and bottom regions of the band to determine the holes (m_h) and electrons (m_e) effective masses. Using these values, the effective density of states of the conduction (N_{CV}) and the valence (N_{VB}) band have been determined at a temperature of 300 K. In semiconductor materials, the carrier scattering time (τ) at a temperature of 300 K is typically between 10^{-13} and 10^{-14} s. In the present study, the mobility of electrons (μ_e) and holes (μ_h) was determined for $\tau = 10^{-14}$ seconds. This is consistent with previous experimental and simulation-based results, as reported in [101, 106–114]. It is worth noting that all the formulas and calculation methods required to determine electron and hole mobilities are briefly given below. Using this method, it is possible to obtain more accurate information about the conductivity features and thermal behavior of K_3SeI.

$$\text{Hole}\Big/\text{electron effective mass}: \quad m^* = h^2\left[\frac{\partial^2 E(k)}{\partial k^2}\right]^{-1} \tag{17}$$

$$\text{Conduction Band of states}: \text{NCB} \quad = \quad 2\left[\frac{2\pi m_e^* K_B T}{h^2}\right]^{\frac{3}{2}} \tag{18}$$

$$\text{Valence Band of states}: \text{NVB} \quad = \quad 2\left[\frac{2\pi m_h^* K_B T}{h^2}\right]^{\frac{3}{2}} \tag{19}$$

$$\text{Hole}\Big/\text{electron mobility}: \mu = \frac{e\tau}{m^*} \tag{20}$$

Here e is the charge of the electron and K_B is the Boltzmann constant [101,106–114]. The values of the m_h, N_{CB}, N_{VB}, and m_e calculated from the data on band gap structures shown in Fig. 4(a) (GGA-PBE) are shown

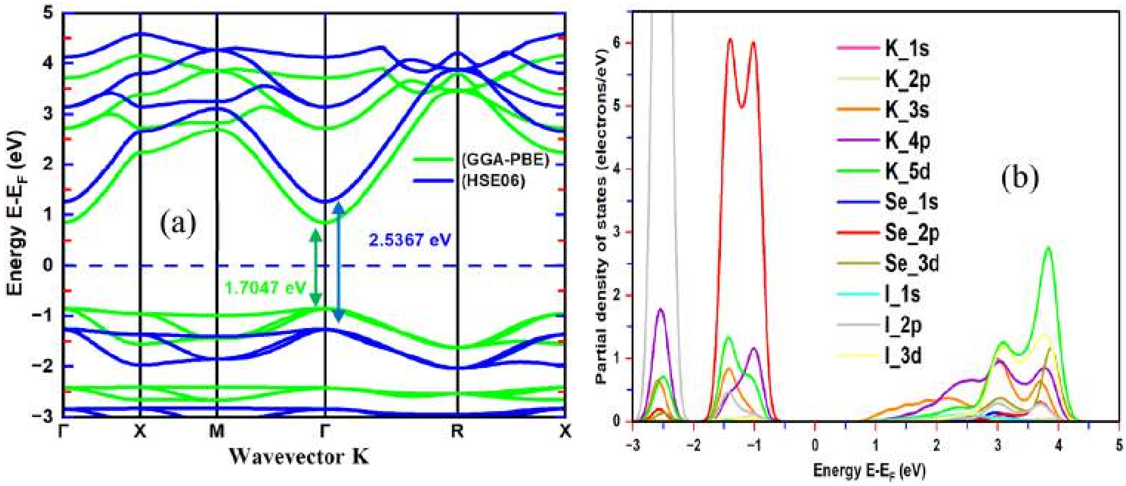

Fig. 4. (a) Band structure and (b) partial density of states of the K_3SeI anti-perovskite.

Table 4
Electronic transport properties of K_3SeI anti-perovskite.

Structure	Hole effective mass, m_h*	Electron effective mass, m_e*	VB effective DOS, N_{VB} (1/ cm^3)	CB effective DOS, N_{CB} (1/ cm^3)	Hole mobility, μ_h (cm^2/Vs)	Electron mobility, μ_e (cm^2/Vs)
K_3SeI	2.0612 m_0	0.4174 m_0	7.39×10^{19}	6.75×10^{18}	8.53	42.2

in Table 4. These values were analyzed to determine the simulated photovoltaic efficiency of K_3SeI absorber-based solar cells.

The electronic transport properties of K_3SeI anti-perovskite are presents in Table 4. Through band structure analysis and parabolic fitting, the hole and electron effective masses have been determined to be $m_h = 2.0612\ m_o$ and $m_o = 0.4174\ m_e$. Here, it can be seen that the effective mass of the electron is about 5 times smaller than that of the hole, indicating that the electron is much more mobile than the hole. As a result, the electron mobility $\mu_e = 42.2\ cm^2/V.s$ and the hole mobility $\mu_h = 8.53\ cm^2/V.s$. This high electron mobility is mainly due to their small effective mass, which is clearly supported by the curvature of the band edge and the parabolic approximation. This trend is also seen in the DOS analysis. The effective DOS of the valence band, N_{VB} ($7.39 \times 10^{19}\ cm^{-3}$) is about 10 times higher than that of the conduction band, N_{CB} ($6.75 \times 10^{18}\ cm^{-3}$). This means that although the number of holes is higher than that of electrons, their mobility is lower, which creates a clear asymmetry in the conduction properties. On the other hand, electrons with lower DOS and smaller effective mass are transported more efficiently as the main charge carriers. In summary, the analysis of Table 4 shows that electrons are much more mobile and efficient than holes, the main charge carrier, in K_3SeI anti-perovskites. This feature is helpful in improving charge transport in K_3SeI-based solar cells and can play a critical role in increasing the power conversion workability of the system. Additionally, this information suggests that the difference in high electron mobility and effective mass can be used in device design and determining appropriate doping strategies. Therefore, the electronic features of K_3SeI component make it optimal for high-performance photocatalysis, photodetector, and solar cell applications [115–118].

3.5.4. *Electrostatic potential profile of (001) slab surface of the K_3SeI anti-perovskite*

The electrostatic potential of the K_3SeI component was calculated using the optimized slab structure presented in Fig. 5(a). The computed values are summarized in Fig. 5(b) and Table 5. These parameters are essential for evaluating whether the valence and conduction band edges are appropriately aligned with the water redox potentials for water splitting, which is crucial for photocatalytic water splitting (hydrogen and oxygen evolution).

Accurate knowledge of the work function and band edge positions is also critical for photovoltaic and optoelectronic devices, as they directly influence charge transfer efficiency, carrier injection, and overall device performance. The mathematical formulations used to estimate these electronic properties from the slab model are provided below [119,120].

Table 5
Comparison of electrostatic potential characteristics of K_3SeI and related materials.

Anti-perovskite Structure	Vacumm level energy (eV)	Ionization energy, IE (eV)	Work Function, ϕ (eV)	Electron affinity, χ (eV)	Reference
Na_3SI	5.089	3.839	3.1717	3.839	[1]
K_3SeI	4.574	3.722	2.637	3.722	This work
Na_3SBr	4.8380	3.570	2.943	3.570	[2]
Cs_2TiI_6	-	6.06	-	4.98	[121, 122]
Cs_2TiBr_6	-	7.13		4.64	[121, 123]
WS_2		5.38	4.75	4.11	[124]
PEA_2SnI_4	-	5.15	4.67	2.98	[125]
TiO_2	-	-	4.13	-	[126]
ZnO	-	-	5.076	-	[127]

$$\text{Work Function: } \phi = E_{vacumm} - E_{Fermi} \tag{21}$$

$$\text{Electron affinity: } \chi = E_{vacumm} - E_{CBM} \tag{22}$$

$$\text{Ionization energy: IE} = E_{vacumm} - E_{VBM} \tag{23}$$

Where E_{VBM} and E_{CBM} are the valence band maximum and conduction band minimum, respectively [119,120]. Table 5 presents the electrostatic potential of K_3SeI element in comparison with other known compounds. The vacuum level energy of K_3SeI is determined to be 4.574 eV, $\chi = 3.722$ eV, $\phi = 2.637$ eV, and IE $= 3.722$ eV. The work function of K_3SeI is significantly lower than that of other anti-perovskites and halide/oxide compounds, indicating that it is highly advantageous in injecting and transporting electrons. The low work function and high electron affinity values of K_3SeI indicate that it is suitable for charge injection and transport in photovoltaic and optoelectronic devices. In addition, the hole transport efficiency can be easily controlled due to the ionization energy value. In comparison, K_3SeI is more effective in electron transport and charge transfer to the conduction band, as the electron affinity of K_3SeI is slightly lower. These properties prove it to be a promising component for efficient charge

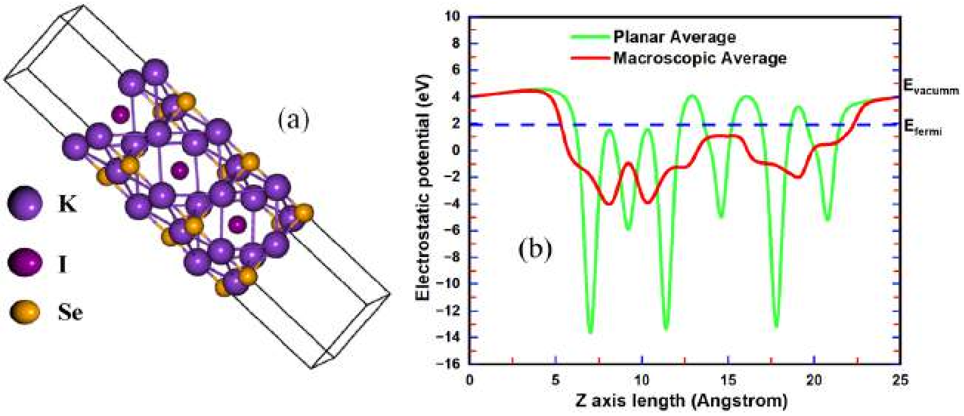

Fig. 5. (a) Optimized slab configuration and (b) electrostatic potential profile of K_3SeI anti-perovskite.

transport, energy conversion, and multifunctional optoelectronic applications. In summary, the comparative analysis in Table 5 shows that the electrostatic potential characteristics of K_3SeI element ensure high performance and device compatibility compared to other anti-perovskite and halide compounds, making it optimal for utilize in next-generation solar cells, photodetectors, and photocatalytic systems [119,120].

3.5.5. Band-edge alignment of K_3SeI anti-perovskite with water redox potentials

The CBM and VBM energy of the vacuum level [128–132],

$$\mathrm{ECBM} \quad (\mathrm{Vacuum}) \quad = \quad - \quad \chi \quad - \frac{E_g}{2} \tag{24}$$

$$= \quad - \quad 3.722 \quad - \quad \frac{1.7047}{2}$$

$= -\ 4.5743$ eV

$$\mathrm{EVBM} \quad (\mathrm{Vacuum}) \quad = \quad - \quad \chi \quad + \frac{E_g}{2} \tag{25}$$

$$= \quad - \quad 3.722 \quad + \quad \frac{1.7047}{2}$$

$= -2.8696$ eV

From the relationship of water redox potential with pH value [128–133].

HER $= -4.44 + \mathrm{pH} \times 0.059$ eV for H+ /H2

OER $= -5.67 + \mathrm{pH} \times 0.059$ eV for O2/H2O

When pH $= 7$

HER $= -4.03$ eV for H+ /H2

OER $= -5.257$ eV for O2/H2O

The VBM and CBM are from the vacuum level in the NHE scale, [131–133]

$^{NHE}E_{CBM}$ (Vacuum) $= -\ 4.5743 + 4.03$ eV

$= -\ 0.5443$ eV ($^{NHE}E_{CBM}$ (Vacuum) < 0 HER is possible)

$^{NHE}E_{VBM}$ (Vacuum) $= -\ 2.8696 + 5.257$ eV

$= 2.3874$ eV ($^{NHE}E_{VBM}$ (Vacuum) > 1.23 eV OER is possible [131-133])

The band edge alignment shown in Fig. 6 clearly shows that both the CBM and VBM of K_3SeI inorganic anti-perovskite at neutral conditions (pH = 7) are well aligned with the redox potentials required for water splitting. This favorable band alignment indicates that the material could act as a potential photocatalyst capable of efficient generation of oxygen and hydrogen using visible light. The estimated uncertainty in the calculated band positions due to DFT limitations and vacuum-to-NHE conversion is typically ±0.2 eV. In particular, the location of the CBM below the H^+/H_2 reduction level and the location of the VBM above the O_2/H_2O oxidation level facilitate the separation of charge carriers and their contributation in redox reactions after the formation of hole-electron pairs. As a result, the electrical behaviour of K_3SeI establish it as a viable candidate for solar-to-hydrogen (STH) conversion technology. Overall, the energy levels required for water splitting are well matched with the correct band position, the ability to respond to visible light, and the inherent chemical stability of the inorganic anti-perovskite class. These three factors together identify K_3SeI as a promising and effective photocatalytic material, which is capable of playing a significant role in green hydrogen (H_2) production [128–133].

3.6. Optical behaviour of K_3SeI anti-perovskite

Perovskite and anti-perovskite-based compounds have gained special importance in modern optical and electronic technologies due to their exceptional light-matter interactions. When light falls on a solid, it exhibits various optical reactions, including reflection, absorption, penetration depth, and energy loss, which are directly connected to the electronic structure and bonding properties of the element [134–136]. The present study investigated several important optical parameters of the K_3SeI anti-perovskite compound, such as imaginary and real components dielectric behaviour, reflectance, refractive, optical energy loss, extinction coefficient, and related spectroscopic behavior, which have been thoroughly analyzed. A detailed evaluation of these properties suggests that K_3SeI can act as an active optical material in terms of light absorption and transport capabilities. Moreover, its moderate real dielectric constant with appreciable frequency dependence, along with suitable visible-light absorption and low electronic losses, makes this material promising for high-performance solar cells and photocatalytic hydrogen production. As a result, the K_3SeI anti-perovskite compound can be considered a promising candidate for advanced renewable energy technologies and photosensitive devices [22,93,137–143].

3.6.1. Dielectric behaviour of K_3SeI anti-perovskite

The dielectric function, $\varepsilon(\omega)$, serves as a fundamental characteristic for understanding the optical behavior of compound. It is conventionally divided into two components: the real part, $\varepsilon_1(\omega)$, which indicates the material's ability to store electric energy, and the imaginary part, $\varepsilon_2(\omega)$, which corresponds to energy absorption within the material [144,145].

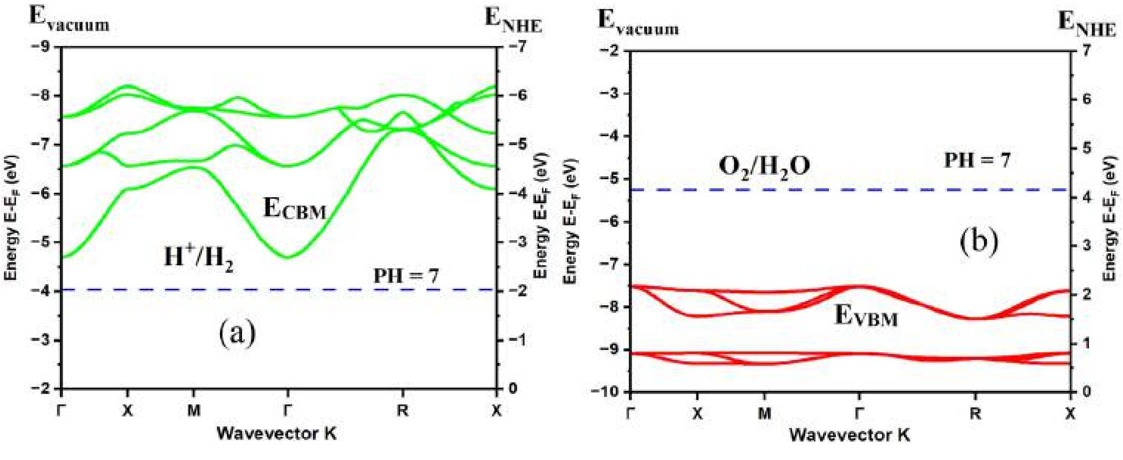

Fig. 6. Alignment of the K_3SeI anti-perovdkite (a) conduction and (b) valence bands with H_2O redox potentials.

The magnitudes of these components vary with the frequency (ω) of incident light, reflecting how the material responds to electromagnetic radiation at different energies. To obtain accurate values of the dielectric function across a frequency range, the Kramers-Kronig relations are frequently employed, allowing a self-consistent calculation of $\varepsilon_2(\omega)$ and $\varepsilon_1(\omega)$ [131]. The imaginary component, $\varepsilon_2(\omega)$, is particularly significant because it directly relates to electronic transitions between bands close to the Fermi level, making it an important indicator for estimating the electronic bandgap of the component. The complete set of dielectric parameters, including $\varepsilon_1(\omega)$, $\varepsilon_2(\omega)$, and $\varepsilon(\omega)$, is typically calculated using established theoretical formulas derived from the compound electronic structure and interband transition probabilities [144–148]. These calculations provide critical insights into how the K_3SeI component interacts with light, forming the basis for calculating its potential in optoelectronic, photovoltaic, and photonic applications.

$$\text{Dielectric function: } \varepsilon(\omega) = \varepsilon_1(\omega) + i\varepsilon_2(\omega) \tag{26}$$

$$\text{Real part of dielectric function} : \varepsilon_1 \quad (\omega) \quad = 1 + \quad \frac{2}{\pi} P \int_0^\infty \frac{\varepsilon_2(\omega')\omega'}{\omega'^2 - \omega^2} d \quad \omega \tag{27}$$

$$\text{Imaginary part of dielectric function} : \varepsilon_2 \quad (\omega)$$

$$= \frac{Ve^2}{2\pi h m^2 \omega^2} \int d^3K \sum | < \quad \varphi_c | p | \varphi_v > |^2 \delta(\quad E_c - E_v - h\omega \quad) \tag{28}$$

Where P is the prime number of the integer. According to the $\varepsilon_1(\omega)$ spectrum shown in Fig. 7(a), it can be seen that the real dielectric function of K_3SeI anti-perovskite increases compositionally starting from a value of about 2.064 and reaching a maximum value around 4 eV. After this, $\varepsilon_1(\omega)$ gradually decreases and enters the negative region at photon energies of 6–8 eV, indicating that the material may exhibit metallic-like reflective behavior at this photon energy. At high frequencies, $\varepsilon_1(\omega)$ gradually returns to the positive side. This behavior indicates that the material exhibits an active dielectric response in the low-energy visible light region, which is very important for optoelectronic technologies and solar cell applications. From the $\varepsilon_2(\omega)$ spectrum in Fig. 7(b), it can be seen that there are several clear peaks in the photon energy range of 1.5–6 eV. The maximum peak is observed near 5 eV. These peaks indicate that significant interband electronic transitions are occurring in K_3SeI, which is mainly due to the transition of electrons from the valence to the conduction band. The high value of $\varepsilon_2(\omega)$ proves that the K_3SeI element has strong light absorption capability in this energy range. Analysis of Fig. 7 suggests that the dielectric function properties of K_3SeI anti-perovskite establish it as a very promising component for efficient light absorption, charge transport, and optoelectronic/photonics applications. In particular, its strong absorption ability in the visible light and UV region makes it useful in photocatalysis, photovoltaics, and optoelectronic devices.

According to Table 6, the dielectric constant $\varepsilon_1(0)$ of K_3SeI anti-perovskite is 2.064, which is slightly lower than that of Na_3SI (2.917) and Na_3SBr (2.62), indicating that its dielectric polarizability is relatively low. However, the high-frequency dielectric constant $\varepsilon_1(\infty)$ of 0.98, which is slightly higher than that of Na_3SI (0.95), shows that the electronic response of K_3SeI is stable to high-frequency light. The first critical point of $\varepsilon_2(\omega)$ is located at 1.7047 eV, which is relatively low, indicating that it is capable of absorbing low-energy photons, hence suitable for visible and near-infrared applications. Ca_3AsBr_3 and Ca_3AsI_3 have much higher $\varepsilon_1 0)$ (4.75 and 5.65), indicating that K_3SeI is relatively less polarizable, but $\varepsilon_1(\infty)$ is almost the same, making it useful in high-frequency optical devices. The dielectric constants of Na_3OI and K_3OI are comparable to those of K_3SeI, which is useful in materials selection. Overall, K_3SeI exhibits moderate static dielectric behavior and a stable high-frequency response, indicating potential applications in optoelectronic devices, photodetectors, and low-energy optical applications. This comparative analysis is consistent with previously published work and is helpful in evaluating the dielectric and optical potential of K_3SeI [144–148].

3.6.2. *Absorption, refraction, reflection, and extinction of K_3SeI anti-perovskite*

It is very important to analyze the optical features of the K_3SeI component in detail, because they largely determine how effective the light-matter interaction will be. Knowing the absorption, refraction, reflection, and extinction behavior of a material can help us understand how much light of a given wavelength can penetrate and in which part the energy is lost. Absorption capacity needs to be evaluated to understand how efficiently the material can absorb solar light energy, which is very important in solar cells and photoelectrochemical systems. The

Table 6
Comparison of dielectric response of K_3SeI anti-perovskite to earlier research findings.

Construction	Static dielectric constant, $\varepsilon_1(0)$	High-frequency dielectric constant, $\varepsilon_1(\infty)$	Initial critical point position of, $\varepsilon_2(\omega)$ (eV)	Reference
Na_3SI	2.917	0.95	2.5	[1]
K_3SeI	2.064	0.98	1.7047	This work
Na_3SBr	2.62	0.78	2	[2]
Na_3OI	2.62	0.94	2	[64]
K_3OI	2.34	0.96	1.05	[65]
Ca_3AsBr_3	4.75	1.65	1.97	[92]
Ca_3AsI_3	5.65	1.6	1.58	[98]

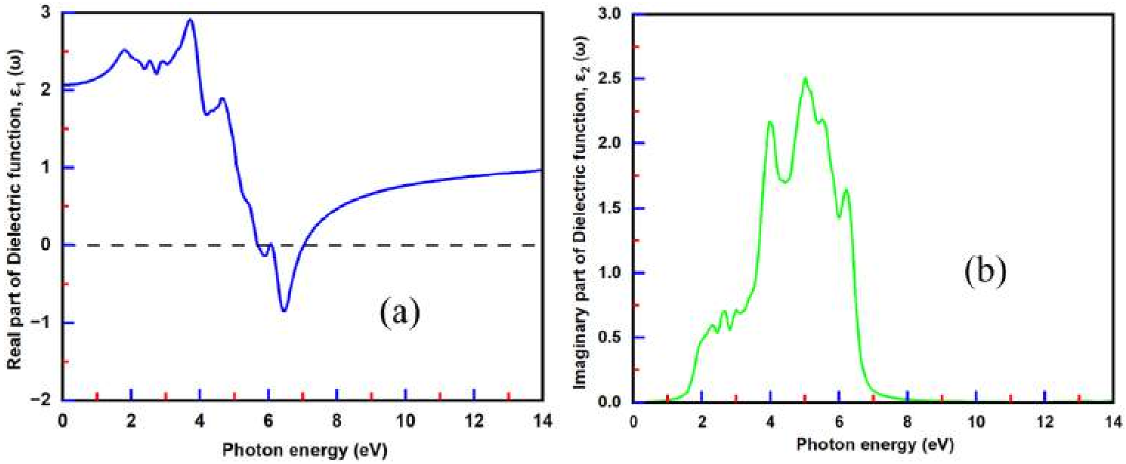

Fig. 7. Dielectric response of K_3SeI anti-perovskite: (a) real component and (b) imaginary component.

value of refraction determines how much light will bend or be guided within a material, so it plays an important role in the design of waveguides, sensors, and optical coatings [149–152]. Reflectance analysis tells us how much light is being lost due to surfaces and how to reduce it and increase light-blocking ability. The extinction coefficient helps to collectively describe the total loss of light from both absorption and scattering. Considering these optical properties together allows us to properly evaluate the potential of the K_3SeI material, especially in determining its applicability in photovoltaic energy conversion, optoelectronic devices, photocatalysis, and future photonic technologies. The various precise mathematical formulas have been applied to understand the light-matter interaction of matter, which helps to measure and explain the effects of absorption, refraction, reflection, and extinction [38,43,76,98,102,119,153,154].

$$\text{Absorption coefficient}: \quad \alpha(\omega) = \frac{\sqrt{2}\omega}{c}\left[\sqrt{\varepsilon_1^2(\omega)+\varepsilon_2^2(\omega)} - \varepsilon_1(\omega)\right]^{\frac{1}{2}} \tag{29}$$

$$\text{Extinction coefficient}: \text{K}(\omega) = \left[= \frac{\sqrt{\varepsilon_1^2(\omega)+\varepsilon_2^2(\omega)} \quad - \varepsilon_1(\omega)}{2}\right]^{\frac{1}{2}} \tag{30}$$

$$\text{Refractive index}, \text{n}(\omega) = \left[= \frac{\sqrt{\varepsilon_1^2(\omega)+\varepsilon_2^2(\omega)} + \varepsilon_1(\omega)}{2}\right]^{\frac{1}{2}} \tag{31}$$

$$\text{Reflectivity}, \text{R}(\omega) = \frac{(n(\omega)-1)^2 + k^2}{(n(\omega)+1)^2 + K^2} \tag{32}$$

Fig. 8(a) shows the dispersive absorption coefficient of the material in the wavelength region 100–900 nm. It can be seen that the element exhibits very powerful absorption properties in the UV wavelength region (100–380 nm). The maximum peak is around 6.8×10^5 cm^{-1} and it is located in the range of 150–250 nm. This high absorption indicates that the interband electronic transition of the material is very active and UV light is almost completely absorbed. Due to its high UV absorption, it can be considered as a useful material for UV photodetectors, UV shielding coatings, and UV optical devices. In the visible region (380–750 nm), the absorption is about $0.5–1 \times 10^5$ cm^{-1}, indicating moderate absorption. After 750 nm (infrared region), absorption drops to almost zero. Notably, the absorption onset appears close to the calculated PBE band gap value of 1.7047 eV (≈728 nm), demonstrating good consistency between the electronic band structure and optical response. This indicates that the way light interacts with the material is mostly controlled by direct electronic transitions between energy bands, making it a potential candidate for high-performance solar cells and photocatalysis. It can help allow most of the visible light to enter the cell by reducing unwanted reflection. Excitonic effects are not explicitly included in the present PBE-based optical calculations. Nevertheless, considering the relatively high absorption coefficients and the dominance of direct electronic transitions, the influence of excitonic binding near the absorption edge is expected to be limited. Therefore, the main optical features and absorption trends obtained here provide a reliable qualitative description of the material's light-harvesting capability.

Next, the spectral behavior of the extinction rate of the material is shown in Fig. 8(b). K(ω) achieves its highest value in the UV light wavelength region (≈ 1.07), indicating strong interband transitions and high optical attenuation. In the visible region, K(ω) decreases significantly (≈ 0.15–0.27) and in the long-wavelength IR region, it

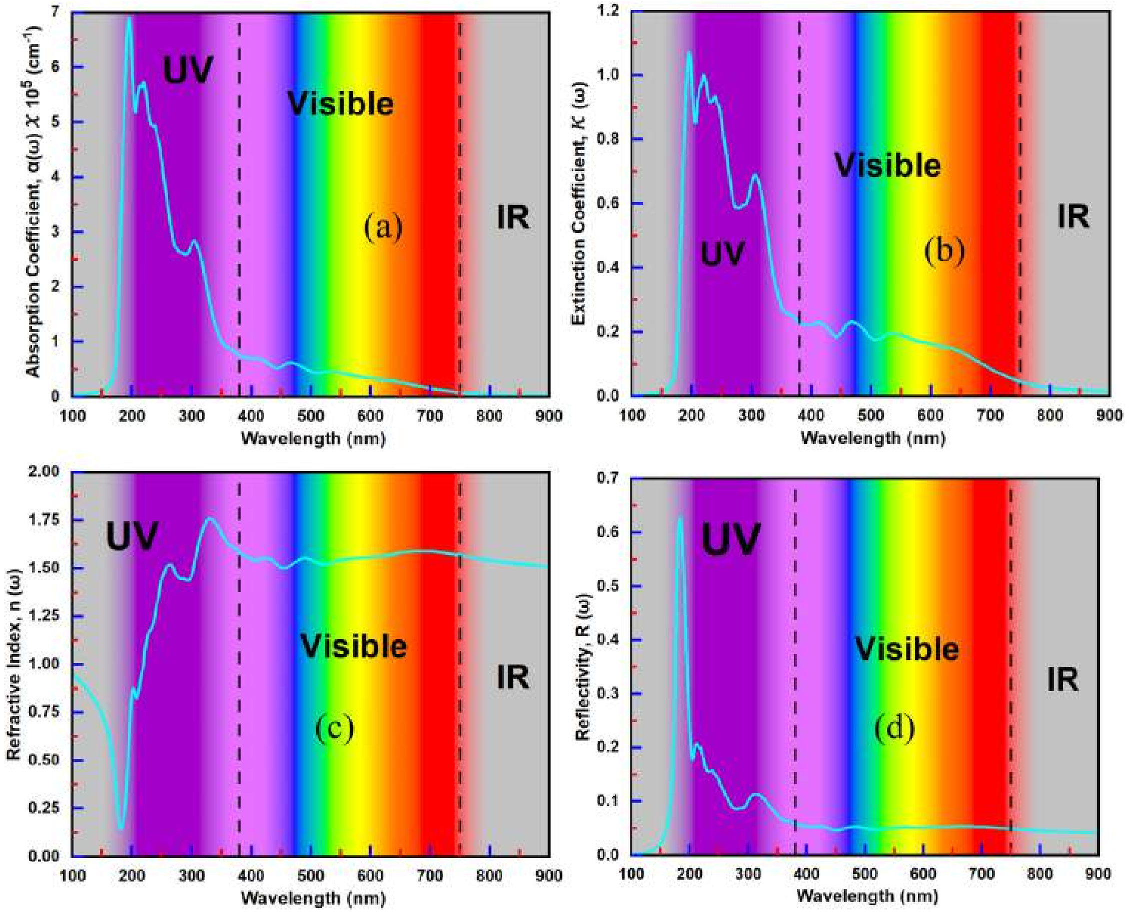

Fig. 8. Dispersive optical characteristics of K_3SeI anti-perovskite: (a) absorption, (b) extinction, (c) refractive, and (d) Reflection.

approaches zero. This trend reveals the K_3SeI element's strong light-absorption ability in the UV range and low extinction in the visible and IR regions. Its value fluctuates with the light wavelength of the photon, rendering it more advantageous in optical device applications. This is beneficial in the design of numerous optical components, including photodetectors, photovoltaics, and photocatalysis.

After that, in Fig. 8(c), it is seen that the refractive index increases rapidly in the UV region to a high value (≈0.98–1.75), reflecting strong electronic polarization. In the visible region, n(ω) remains remarkably stable (≈1.5–1.56), indicating less dispersive behavior. In the IR region, n(ω) gradually decreases to about 1.4. This spectral refractive response of the material characterizes it as an optically stable and low-dispersion semiconductor. This n(ω) property makes the material useful as a photovoltaic, photocatalytic, and optoelectronic, or lens material.

And, the reflectivity in Fig. 8(d) clearly shows differential behavior in three regions: high reflectance in the UV region (≈0.15–0.65), significantly lower reflectance in the visible region (≈0.06–0.1), and a slight increase in the IR region (≈0.06–0.12). Low reflectivity in the visible region indicates high optical transmission ability of the material, while high reflectivity in the UV region is a result of its increased surface electronic response. The design of solar cells, lenses, photonic devices, optical filters, and waveguides filters is crucial. K_3SeI exhibits pronounced dispersion characteristics contingent upon the value of n(ω), indicating its potential use in nonlinear optics and laser technologies.

The optical behaviour shown in Fig. 8, strong UV absorption, low optical loss, stable refractive index, and low reflectivity in the visible light wavelength region, indicate that the K_3SeI component has great potential for high-efficiency photovoltaic absorbers, light-activated photocatalysts, and optoelectronic devices (sensors, photodetectors, optical coatings, etc.) operating in the UV–visible range [38,43,97,119,153–160].

3.6.3. *Effect of optical depth, energy Loss, optical conductivity, and penetration depth on the optical response of K_3SeI anti-perovskite*

Analyzing the penetration depth, optical depth, optical conductivity, and energy loss of a material is extremely important, as they directly indicate how light and electromagnetic waves penetrate, distribute, and absorb within the material. Penetration depth refers to how far light of a specific wavelength can penetrate a material, which is essential for solar cell absorption layer design or photocatalysis [161–163]. Optical depth indicates how quickly light is absorbed or how much energy is lost through the material, which is important in determining the efficiency and energy loss in light-generating processes [161–163]. Optical conductivity refers to how effective a material is at absorbing light and generating electrical charge, which is important in photovoltaic devices, photodetectors, and other optoelectronic devices [164–169]. Additionally, energy loss analysis can be used to understand how much energy light or radiation is reducing to a material, which is especially helpful in energy conversion processes and thermal management [161]. Considering all this information together, the material light absorption capacity, electron-hole production efficiency, and energy conversion capacity can be determined. As a result, their analysis is essential for the development of solar cells, photocatalysis, optoelectronic sensors, light refraction and absorption, and sustainable energy technologies. The various precise mathematical formulas were applied to understand the light-matter interaction of matter, which helps to measure and explain the effects of optical depth, energy loss, optical conductivity, and penetration depth [164–168].

$$\text{Penetration depth}: \quad \delta(\omega) = \frac{1}{\alpha(\omega)} \tag{33}$$

$$\text{Optical depth}: \quad \tau(\omega) = \alpha(\omega) \times \mathrm{d} \tag{34}$$

$$\text{Optical conductivity}: \quad \sigma(\omega) = \frac{\omega \quad \varepsilon_2(\omega)}{4\pi} \tag{35}$$

$$\text{Energy loss function}: \mathrm{L}(\omega) = \frac{\varepsilon_2(\omega)}{\varepsilon_1^2(\omega) + \varepsilon_2^2(\omega)} \tag{36}$$

Here, the optical depth was carried out assuming the medium to be nearly 8 μm in thickness.

Fig. 9(a) shows the variation of the optical penetration depth δ(ω) as a function of wavelength. In the ultraviolet region (100–400 nm), the penetration depth is extremely small, indicating that UV photons are absorbed very close to the surface, confirming the strong absorption behavior observed in Fig. 8(a). This strong UV absorption is primarily due to interband electronic transitions from valence band states dominated by Se-p and I-p orbitals to conduction band states dominated by K-s and Se-s orbitals, as supported by the PDOS analysis, which is shown in Fig. 4(b). In the visible wavelength range (400–700 nm), the penetration depth increases gradually but remains within the sub-micron range. Notably, this penetration depth is significantly smaller than the absorber thickness of 1–2.5 μm employed in the SCAPS-1D device simulations. This indicates that the absorber layer is optically thick enough to ensure efficient absorption of visible photons well within the active region, thereby supporting effective photogenerated charge carrier collection. In the infrared region (700–900 nm), the penetration depth increases considerably due to reduced absorption at photon energies below the band gap, allowing longer-wavelength photons to penetrate deeper into the material. This behavior is consistent with the electronic structure of the material and the absorption trends discussed earlier.

The optical depth τ(ω), shown in Fig. 9(b), is very high in the UV region, reflecting rapid energy dissipation, consistent with the strong absorption. In the visible spectrum, τ(ω) is relatively low, allowing light to travel longer distances, which is advantageous for charge carrier generation. In the IR region, τ(ω) decreases again, indicating that energy loss is relatively low for longer wavelengths. These trends highlight the material's capacity for efficient absorption and energy dissipation across the spectrum.

Fig. 9(c) depicts the optical conductivity σ(ω), which is maximum in the UV region, confirming that the material effectively converts absorbed photons into charge carriers. In the visible region, σ(ω) is slightly lower but still significant, while in the IR region it is minimal, indicating low charge carrier generation at longer wavelengths. These results are relevant for modeling the light absorption and carrier generation in SCAPS-1D simulations, directly influencing the short-circuit current (J_{sc}) and device efficiency.

The energy loss function L(ω), plotted in Fig. 9(d), peaks in the UV region, indicating strong interaction of electrons and photons with the material and higher energy dissipation. In the visible and IR regions, L(ω) decreases, suggesting lower energy loss and more efficient transport of light and carriers.

An optical thickness of 8 μm was assumed in the SCAPS simulations to account for full absorption of the incident light, which is within the experimentally feasible range for anti-perovskite thin films. This choice ensures that the simulated device captures the material's optical behavior realistically and allows for proper evaluation of photocurrent generation.

In summary, these analyses demonstrate that K_3SeI exhibits strong UV absorption due to interband transitions, efficient visible light absorption for photogenerated carrier collection, and minimal IR absorption. Compared to known UV-active materials such as TiO_2 and ZnO, K_3SeI shows comparable UV absorption efficiency, indicating its potential for UV-driven optoelectronic applications. These findings provide crucial insight into the material's performance in SCAPS-1D simulated devices and highlight its suitability for solar cells and other light-absorption-based technologies [155–168].

3.7. *Vacancy defect formation analysis of 2× 2 × 1 supercell of K_3SeI anti-perovskite*

Vacancies are the most common point defects in crystals, which

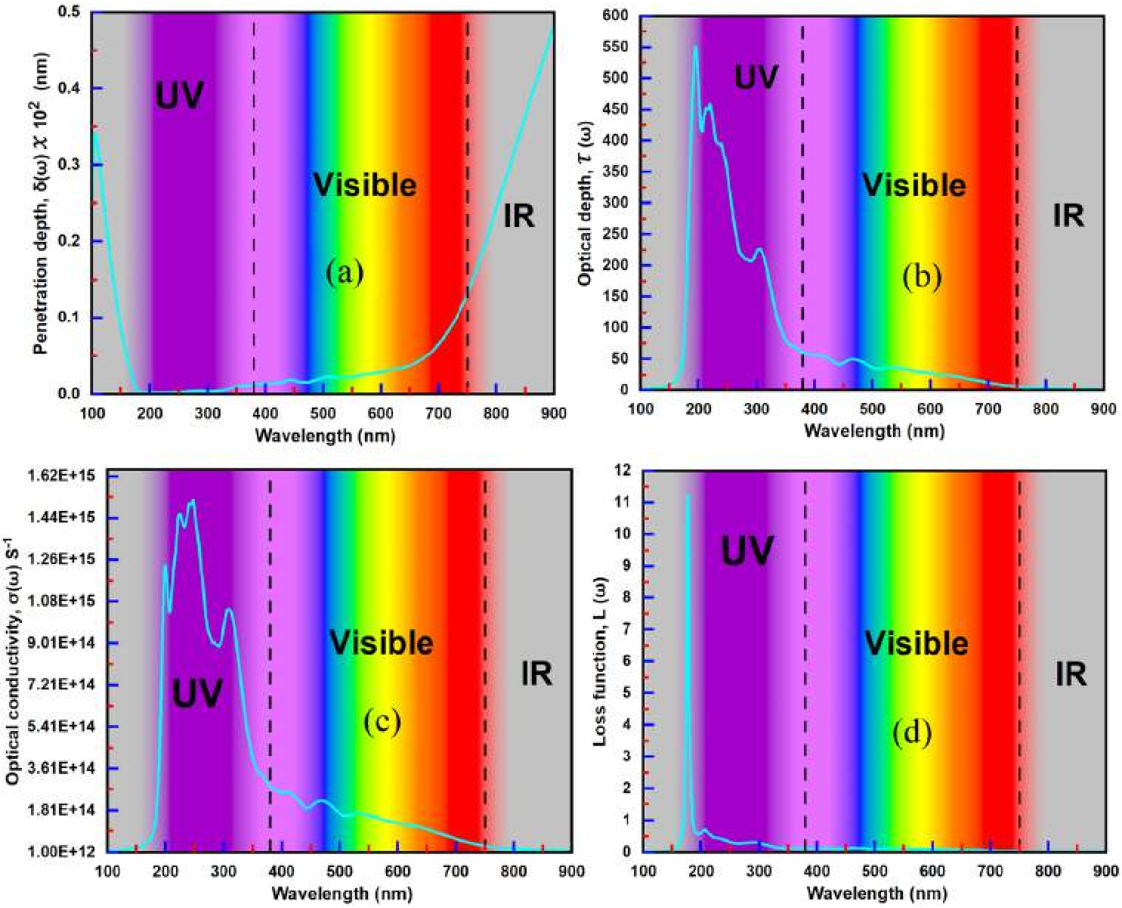

Fig. 9. Detailed optical response of K_3SeI anti-perovskite: (a) light penetration depth, (b) optical attenuation behavior, (c) frequency-dependent optical conductivity, and (d) energy loss spectrum.

significantly affect their structural and electronic properties. In this work, the energy required to form a vacancy defect for a 2 × 2 × 1 supercell of K_3SeI anti-perovskite as seen in Fig. 10 has been analyzed using Eq. (37) [44–48]. According to Table 7, the vacancy formation energy of K is found to be about 6.2 eV, that of Se is about 6.26 eV, and that of I is about 3.0 eV. This result indicates that an iodine atom can form vacancies relatively easily; that is, vacancy formation for an I atom in the crystal is more probable. On the other hand, the vacancy formation energy of K and Se is relatively high, which shows that these atoms are comparatively stable in the crystal structure and the probability of vacancy formation is low. These positive and realistic formation energy values ensure that the simulation performed with the 2 × 2 × 1 supercell is able to accurately capture defect behavior. As a result, this analysis provides important insights into defect engineering and material design of K_3SeI anti-perovskite [44–48].

Formation energy of vacancy, $E_f(V_X)=E_{defect}-E_{perfect}+\Sigma_i n_i \mu_X$ (37)

Where, E_{defect} = Total energy of supercell with one X atom removed.

$E_{perfect}$ = Total energy of perfect supercell.

n_i = Number of remove atom.

μ_X = Chemical potential of atom X (reference).

3.8. Surface energy analysis of the (001) slab structure of K_3SeI anti-perovskite

In this study, the surface energy of the material has been determined using the slab model (001). Eq. (38) has been applied to calculate the surface energy [53–56]. The obtained surface energy (0.000514 eV/A^2 or 0.00824 J/m^2) value is relatively low, which indicates that the surface concerned is thermodynamically stable in nature. In general, low surface energy means that less energy is required to break or form new bonds on the surface. This allows the material to form a specific crystallographic surface more easily and remain stable in its environment. Since the energy difference between the slab and bulk structures is very small, it is understood that the arrangement of atoms used in the slab model is well consistent with the bulk structure. Additionally, no significant additional energy was accumulated due to surface relaxation or reconstruction. That is, no major structural changes occurred at the surface. Overall, the calculated surface energy value provides a reliable idea of the surface stability of the material and creates a solid foundation for future surface-based scientific research [53–56].

$$\text{Surface energy,} \quad \gamma = \frac{E_{Slab} - N \times E_{bulk}}{2 \times A} \tag{38}$$

Where, Total energy of slab, $E_{Slab} = -8633.27$ eV.

Total energy of bulk, $E_{bulk} = -2877.77$ eV.

Number of formula unit of slab structure, N = 3.

Surface area, A = 6.2365 × 6.2365 = 38.8939 Å^2.

E_{bulk} total energy have been calculate k-mesh of 4 × 4 × 4 centered at gamma, 40 ecutwfc, and 240 ecutrho. Also, E_{Slab} total energy have been calculate k-mesh of 4 × 4 × 1 centered at gamma, 40 ecutwfc, and 240 ecutrho.

3.9. Adsorption energy analysis of the (001) slab structure of K_3SeI anti-perovskite

In this study, the surface adsorption energy of the material has been determined using the slab model (001). The data of Table 8 and Eq. (39)

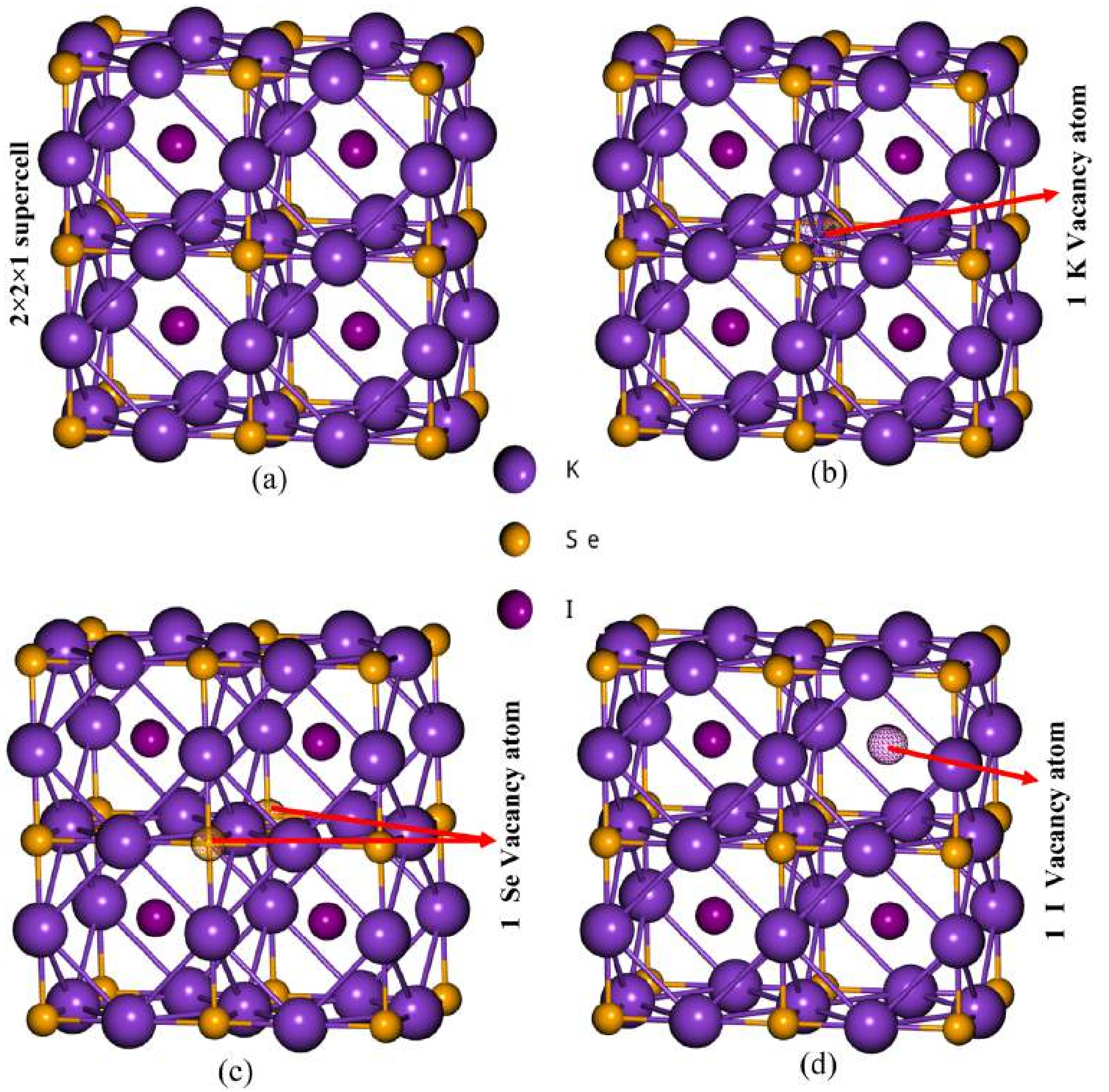

Fig. 10. (a) 2 × 2 × 1 supercell, (b) 1 K atom vacancy supercell, (c) 1 Se atom vacancy supercell, (d) 1 I atom vacancy supercell.

Table 7
Vacancy defect formation energy of 2 × 2 × 1 supercell of the K_3SeI anti-perovskite.

Material	Total energy (Ry)	Total energy (eV)	Atom number	Formation energy (eV)	Formation energy per atom (eV/atom)
E_{defect} (K)	-789.5826	−10743.6	19	6.2	0.3263
E_{defect} (Se)	-827.0776	−11252.6	19	6.26	0.3295
E_{defect} (I)	-823.0373	−11200.0	19	3	0.1579
$E_{perfect}$	-846.2078	−11515.0	20	-	-
μ_K	-56.23588	−765.2		-	-
μ_{Se}	−18.82615	−256.14		-	-
μ_I	−22.9360	−312.0		-	-

Table 8
The total energy and adsorption energy of the (001) slab of K_3SeI anti-perovskite.

Surface/Adsorbate	Total energy (Ry)	$E_{adsorption}$ (eV)
$E_{surface+H}$	-635.5241	−0.583
$E_{surface+O}$	-664.9371	−0.312
$E_{surface+OH}$	-666.3435	−0.228
$E_{surface+OOH}$	-696.7341	−0.453
$E_{surface}$	-634.5401	
E_{H2}	-1.882116	
E_{H2O}	-32.7277	
E_{O2}	-60.7481	

has been applied to calculate the surface adsorption energy [53–56]. The adsorption energies (Eads) given in Table 8 show that each adsorbate is held to the surface to varying degrees of strength. The adsorption energies of H* and O* are −0.27 eV and −0.31 eV, respectively, indicating that these two molecules are relatively less strongly adsorbed to the surface. On the other hand, the adsorption energies of OH* and H* are −0.228 eV and −0.583 eV, respectively, indicating relatively more stable adsorption. This suggests that hydroxyl (OH*) and hydroperoxyl (OOH*) species are more strongly adsorbed to the surface, which may be important as reaction intermediates. Since H* and O* adsorb relatively less strongly, they are able to be easily removed from the surface or react with other species. Overall, the adsorption energy trend is as follows: OH* < O* < OOH* < H*. This trend indicates that the surface is able to hold progressively more complex intermediates, which play an important role in an electrocatalytic or surface reaction context [53–56, 169,170].

$$\text{Adsorption energy, } E_{ads} = E_{surface+adsorbate} - E_{surface} - E_{adsorbate} \tag{39}$$

$$H \text{ adsorption energy, } E_{ads}(H^*) = E_{surfaces+H} - E_{surfaces} - \frac{1}{2}E_{H2} \tag{40}$$

$$O \text{ adsorption energy, } E_{ads}(O^*) = E_{surfaces+O} - E_{surfaces} - \frac{1}{2}E_{O2} \tag{41}$$

$$\text{OH adsorption energy, } E_{ads}(OH^*) = E_{surfaces+OH} - E_{surfaces} - \left(E_{H2O} - \frac{1}{2}E_{H2}\right) \tag{42}$$

$$\text{OOH adsorption energy, } E_{ads}(OOH^*) = E_{surfaces+OOH} - E_{surfaces} - \left(E_{H2O} + \frac{1}{2}E_{O2} - \frac{1}{2}E_{H2}\right) \tag{43}$$

3.10. Free energy and overpotential analysis of the (001) slab structure of K_3SeI anti-perovskite

The Gibbs free energy (ΔG) for the adsorption of reaction intermediates on the surface was calculated using the following Eq. (44) [53–56]. where E_{ads} is the adsorption energy obtained from DFT calculations, (ΔZPE−TΔS) represents the zero-point energy and entropic corrections taken from literature values 0.24 eV, 0.05 eV, 0.35 eV, and 0.32 eV for H*, O*, OH*, and OOH*, respectively, ΔGpH is the free energy correction at pH = 7 (0.4144 eV), and U is the applied potential (set to 0 V in this work). Using these corrections, the free energies of adsorption for H*, O*, OH*, and OOH* were calculated, which is shown in Table 9. These values were subsequently used to construct the free energy diagrams for the HER and OER pathways. The free energy change at each of these reaction steps is calculated using Eqs. (49) to (52) [53–56].

$$\text{Gibbs free energy, } \Delta G = E_{ads} + (\Delta ZPE - T\Delta S) + \Delta G_{PH} - eU \tag{44}$$

The intermediate reaction steps involved in an OER are as follows:

$$* + OH- \rightarrow OH^* + e^- \tag{45}$$

$$OH^* + OH^- \rightarrow O^* + H2O + e^- \tag{46}$$

$$O^* + OH^- \rightarrow OOH^* + e^- \tag{47}$$

$$OOH^* + OH^- \rightarrow O_2 + * + H_2O + e^- \tag{48}$$

The free energy change at each of these reaction steps is calculated using the following expressions:

$$\Delta G_1 = G(OH^*) - G(*) - G(OH^- - e^-) \tag{49}$$

$$\Delta G_2 = G(O^*) + G(H_2O) - G(OH^*) - G(OH^- - e^-) \tag{50}$$

$$\Delta G_3 = G(OOH^*) - G(O^*) - G(OH^- - e^-) \tag{51}$$

$$\Delta G_4 = G(*) + G(O_2) + G(H_2O) - G(OOH^*) - G(OH^- - e^-) \tag{52}$$

$$\text{HER overpotential, } \eta\text{HER} = \frac{|\Delta G_{H^*}|}{e} \tag{53}$$

$$\text{OER overpotential, } \eta\text{OER} = \frac{\max(G_1, G_2, G_3, G_4)}{e} - 1.23 \tag{54}$$

The overpotentials of the hydrogen evolution reaction (HER) and oxygen evolution reaction (OER) on the (001) crystal surface were determined using the values in Table 8 and the Eqs. (53) and (54) [53–56]. In OER, the maximum free energy change is determined by considering four reaction steps (ΔG_1–ΔG_4), and the overpotential is derived from this. ΔG_1, ΔG_2, and ΔG_3 were calculated directly using the Gibbs free energy values of the adsorbate, whereas a relative approach was used for ΔG_4 (since $G(H_2O)$ and $G(O_2)$ energies are not directly included). Using this method, the overpotentials of HER and OER on the (001) surface were found to be 0.071 V and 2.64 V, respectively. This analysis suggests that the (001) surface is highly effective for HER, while a slightly higher overpotential is observed for OER. Fig. 11 shows the (001) surface free energy diagram for OER and HER of the K_3SeI anti-perovskite [53–56,171,172–174].

3.11. Energy band alignment and carrier generation–recombination behavior of the proposed solar cell device

The primary objective of this study is to assess the photovoltaic efficiency and solar-to-hydrogen (STH) production capacity of the K_3SeI material. A device structure comprising Al/FTO/SnS_2/K_3SeI/CuO/Se was devised and computationally simulated utilizing the SCAPS-1D program, as depicted in Fig. 12(a). The principal optoelectronic characteristics of the different layers, specifically FTO, SnS_2, K_3SeI, and CuO, are delineated in Table 10. The interfacial parameters for the proposed single active absorber-based Al/FTO/SnS_2/K_3SeI/CuO/Se configuration are presented in Table 11. Fig. 12(b) shows the energy band alignment across the entire thickness of the proposed FTO/SnS_2/K_3SeI/CuO solar cell. It can be seen from the figure that there is no significant energy barrier for electron transport at the FTO/SnS_2 interface, which facilitates electron collection. The smooth transition of the bands at the SnS_2/K_3SeI interface indicates efficient charge transport and low interface recombination. The large band gap and distinct Fn–Fp positions within the

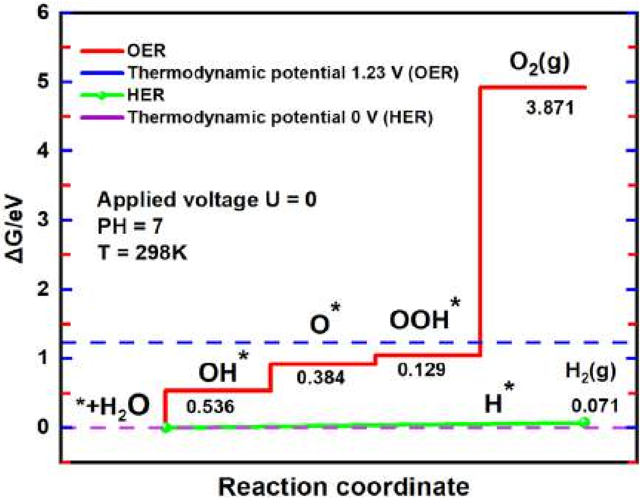

Fig. 11. The (001) surface free energy diagram for OER and HER of the K_3SeI anti-perovskite.

Table 9
The gibbs free energy and reaction path energy of H*, O*, OH*, and OOH* absorbate.

Adsorbate step	ΔG_{H^*}	ΔG_{O^*}	ΔG_{OH^*}	ΔG_{OOH^*}	ΔG_1	ΔG_2	ΔG_3	ΔG_4
value	0.071 eV	0.152 eV	0.536 eV	0.281 eV	0.536 eV	0.384 eV	0.129 eV	3.871 eV

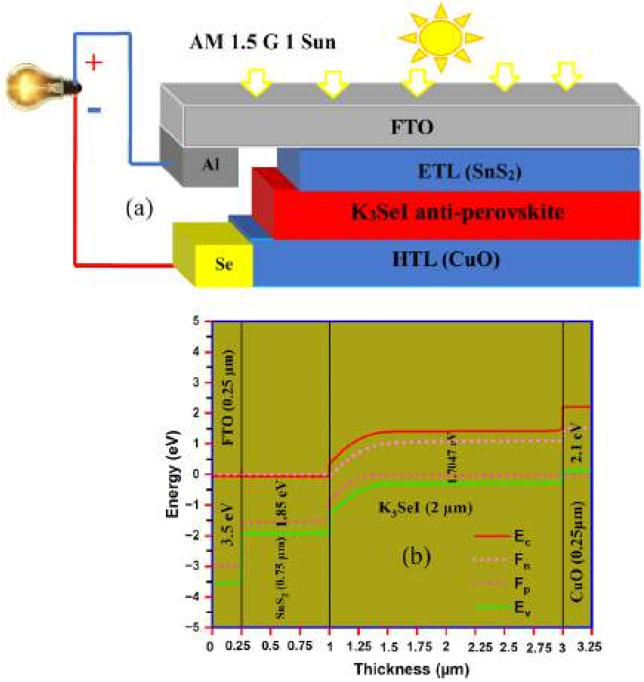

Fig. 12. **(a)** Schematic structure of a solar cell employing K_3SeI anti-perovskite as the absorber layer and (b) Energy band diagram across the entire thickness of the proposed solar cell structure.

Table 10
Optoelectronic parameter of the K_3SeI absorber with FTO, CuO, and SnS_2 elements utilized in SCAPS-1D.

Parameter	SnS_2 [2]	FTO [2]	K_3SeI (This work)	CuO [2]
W_{th} (cm)	0.75*	0.25*	2*	0.25*
Eg (eV)	1.85	3.5	1.7047	2.1
X_e (eV)	4.26	4	3.722	3.2
ε_r	17.7	9	2.064	7.11
N_{CB} (1/cm^3)	7.32E+ 18	2.2E+ 18	6.75×10^{18}	2.2E+ 18
N_{VB} (1/cm^3)	1E+ 19	1.8E+ 19	7.39×10^{19}	1.8E+ 18
V_{te} (cm/s)	1E+ 7	1×10^7	1×10^7	1E+ 7
V_{th} (cm/s)	1E+ 7	1×10^7	1×10^7	1E+ 7
μ_e (cm^2/V.s)	5E+ 1	2E+ 1	42.2	3.4
μ_h (cm^2/V.s)	2.5E+ 1	1E+ 1	8.53	3.4
N_D (1/cm^3)	9.85E+ 19	2E+ 19	0	0
N_A (1/cm^3)	0	0	1E+ 15*	1E+ 20
N_t (1/cm^3)	1E+ 14	1E+ 15	1×10^{15}*	1E+ 15
Absorption data (1/m)			K_3SeI.abs	

* For the preliminary research and simulations, a variable domain approach was employed. The absorption characteristics of the component K_3SeI were extracted and stored in an K_3SeI.abs file, based on the absorption data presented in Fig. 7(a).

Table 11
Interface defect characteristics of the K_3SeI anti-perovskite absorber-based solar cell structure [43].

Parameter	SnS_2/K_3SeI and K_3SeI/CuO
Type of defect	Neutral
Cross section area for electron and hole (cm^2)	1.00×10^{-19}
Energetic distribution	Single
Energy level E_t	Above the highest Ev
Reference Energy E_r (eV)	0.600
Total density (1/cm^3)	1.00×10^{10}

K_3SeI absorber layer ensure clear charge separation. On the other hand, the favorable valence band offset at the K_3SeI/CuO interface facilitates hole transport. As a result, electrons and holes can flow efficiently in opposite directions, which reduces recombination losses. Overall, this favorable band alignment maintains the high charge collection efficiency of the device and is helpful in improving the fill factor and power conversion efficiency. Therefore, K_3SeI absorber can be considered as a suitable material for high-efficiency anti-perovskite solar cells. Fig. 13 (a) shows the carrier generation profile across the entire thickness of the proposed Al/FTO/SnS_2/K_3SeI/CuO/Se solar cell. It can be seen from the figure that the generation is maximum near the illuminated front contact and gradually decreases towards the SnS_2/K_3SeI interface. This trend is largely a result of more photon absorption in the forward direction. Notably, carrier generation is maintained throughout the entire 2 μm thickness of the K_3SeI absorber layer, indicating the strong light absorption and efficient charge generation capabilities of this material. The overall recombination profile of the device is presented in Fig. 13 (b). It can be seen that the recombination is relatively low in the FTO and SnS_2 transport layers but increases within the K_3SeI absorber layer. This phenomenon is mainly due to the higher carrier density in the absorber region. It is noteworthy that, although the maximum recombination value is located inside the absorber, no sharp recombination peak is observed in the interface region, indicating effective charge extraction. Overall, the comparison of the generation and recombination profiles suggests that the generation rate in the K_3SeI absorber layer is significantly higher than that of the recombination. This balance ensures efficient charge collection in the device and plays a crucial role in achieving improved photovoltaic performance. The results clearly indicate that K_3SeI is an effective and promising absorber material in the proposed device structure.

3.12. Analysis of EQE and J–V characteristics for the K_3SeI inorganic anti-perovskite

The main aim of this study is to verify the workability of anti-perovskite solar cells (APSCs) modeled using the K_3SeI anti-perovskite absorber layer shown in Fig. 12(a). The photoelectric conversion results of K_3SeI components are showed in Table 12, where extremely high efficiency can be observed. This K_3SeI components exhibited a J_{sc} of 31.723 mA/cm^2, a FF of 86.65 %, a PCE of 31.20 %, and an V_o of 1.135 V, clearly indicating its remarkable photovoltaic (PV) capabilities. As can be seen from the wavelength versus EQE analysis presented in Fig. 14(a), the proposed K_3SeI material achieved a maximum EQE of 98.98 % in the 350–700 nm region, which bears testimony to its high efficiency in light absorption and charge generation. On the other hand, the J–V features shown in Fig. 14(b) shows a relatively slightly higher J_{sc} and a relatively lower V_o. This trend indicates that the overall workability of the solar cell is further improved due to the high current generation capacity and low voltage loss of K_3SeI.

3.13. Impact of defect density and shallow acceptor concentration in the K_3SeI absorber layer on the photovoltaic performance parameters (PCE, FF, J_{SC}, and V_O) of the proposed anti-perovskite solar cell

Analyzing the defect density of the K_3SeI absorber layer is crucial for understanding the performance of APSCs. Excess defects in the anti-perovskite absorber layer essentially create pinholes, which rapidly reduce the sheet stability and degrade device performance. These defects are mainly divided into two categories based on their location and depth: shallow and deep defects. Shallow defects generally reduce carrier recombination, but deep defects increase charge carrier recombination and weaken the crystal structure [1,2,6,43]. The main types of defects are vacancy: lack of K, Se, or I; interstitial: excess K, Se, or I; and antisite defects: K, Se, or I in another position. Each defect affects the carrier lifetime and mobility differently, which directly affects the PCE, J_{SC}, FF, and V_o of the solar cell. Using Eqs. (55) and (56), we evaluated the performance of the entire structure at different defect densities [1,2,

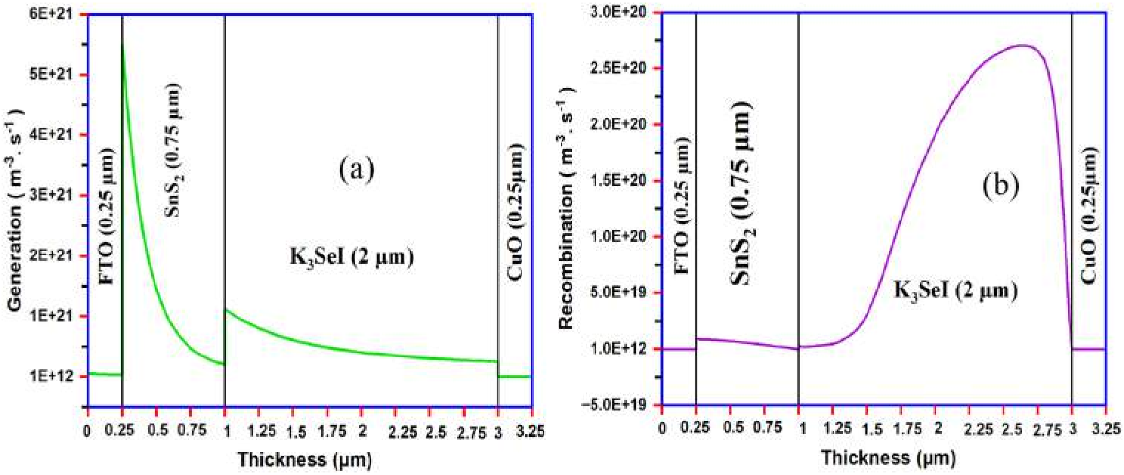

Fig. 13. (a) Carrier generation profile and (b) total recombination behavior across the full thickness of the proposed K_3SeI absorber-based solar cell.

Table 12
The PV paramter of the K_3SeI absorber-based solar cell structure.

structure	J_{sc} (mA/cm^2)	V_o (Volts)	FF (%)	PCE (%)
Al/FTO/SnS_2/K_3SeI/CuO/Se	31.723	1.135	86.65	31.20

6,43]. Adding a small amount of dopant to the absorber layer increases the stability of PSCs and APSCs and also significantly improves performance. The interface layer also helps in improving the PCE of APSC. However, increasing the acceptor concentration also increases the charge carrier recombination. Therefore, choosing the right dopant concentration is very important to maximize the efficiency of the proposed solar cell [1,2,6,43].

$$R_{SRH} = \frac{np - n_i^2}{\tau_p(n + n_i) + \tau_n(p + p_i)} \tag{55}$$

$$\tau = \frac{1}{\sigma N_t V_{th}} \tag{56}$$

Here, n and p indicate the concentration of electrons and holes, respectively. τ_n and τ_p indicate the lifetime of electrons and holes; N_t expresses the total defect concentration; V_{th} indicates the thermal velocity; and p_i and n_i indicate the intrinsic concentrations of holes and electrons, respectively. In the equation, τ indicates the carrier lifetime [1,2,6,43]. In this optimization, solar cells with K_3SeI-based absorber layers were analyzed, where the absorber layer defect density and shallow acceptor concentration were changed while keeping all other parameters unchanged. According to the proposed APSC structure (Fig. 12), the absorber layer defect density has been varied from 10^{12} to 10^{18} (1/cm^3), and the shallow acceptor density has been varied from 10^{12} to 10^{18} (1/cm^3). The optimization results are presented in Fig. 15, which is applicable to K_3SeI absorber-based APSCs. This study has shown that K_3SeI absorber-based APSC is a high-efficiency solar cell device, which provides improved performance. Fig. 15 shows that PCE, FF, J_{SC}, and V_o increase as the shallow acceptor density increases, and PCE, FF, J_{SC}, and V_o decrease as the defect density increases. However, very high defect density and high shallow acceptor density are not acceptable for optimal solar cell devices [1,2,6,43]. Therefore, we choose that the shallow acceptor density of 10^{15} (1/cm^3) and defect density of 10^{15} (1/cm^3) yield the best photovoltaic results. This investigation of the defect density and shallow aceptor density of the absorber layer of K_3SeI gave the best result, with a J_{sc} of 31.723 mA/cm^2, an FF of 86.65 %, a PCE of 31.20 %, and a V_o of 1.135 V.

3.14. Impact of electron and hole mobility in the K_3SeI absorber layer on the photovoltaic performance parameters (PCE, FF, J_{SC}, and V_O) of the proposed anti-perovskite solar cell

In this study, the electronic, optical, and thermoelectric properties of a new K_3SeI anti-perovskite material were determined using DFT-based methods. Based on previous studies, the electron and hole mobilities of the K_3SeI absorber are found to be 42.2 cm^2/V.s and 8.53 cm^2/V.s, respectively, with a carrier relaxation time of approximately

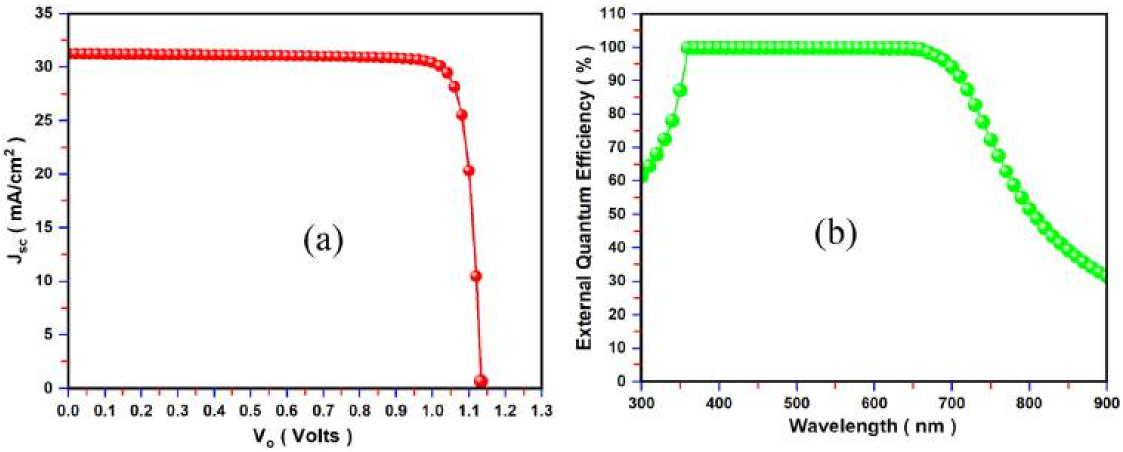

Fig. 14. (a) J–V response and (b) external quantum efficiency spectrum of the proposed K_3SeI anti-perovskite solar cell.

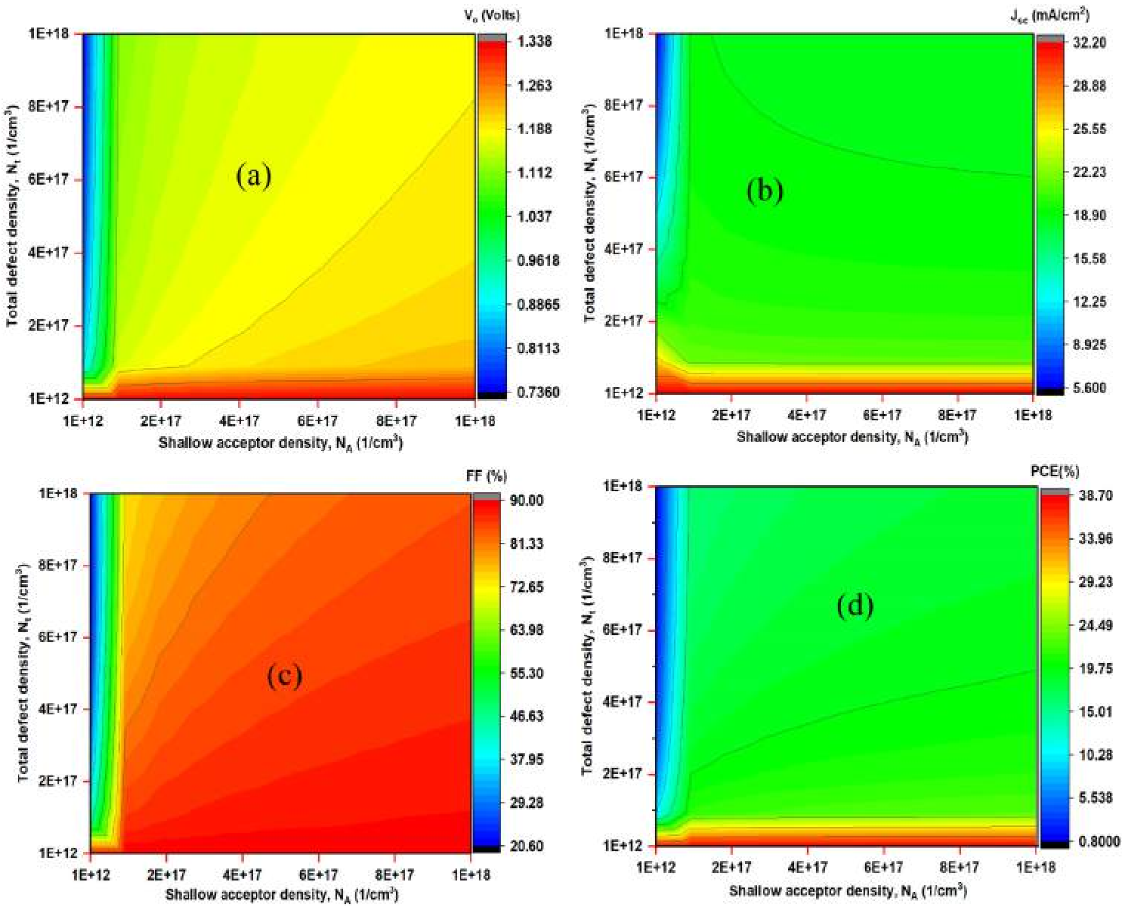

Fig. 15. Influence of shallow acceptor concentration and bulk defect density in the K_3SeI absorber layer on (a) V_O, (b) J_{SC}, (c) FF, and (d) PCE of the proposed anti-perovskite solar cell.

$t = 1 \times 10^{-14}$ s. Since changing the carrier relaxation time also changes the electron and hole mobility, the performance of the solar cell structure in SCAPS-1D was tested by changing the mobility of the K_3SeI absorber layer to different values. The electron and hole mobility varied from 5 to 100 cm^2/V.s, and it was found that the carrier mobility of the absorber layer directly affects the PCE, J_{sc}, FF, and V_o of the solar cell. The optimization results are presented in Fig. 16, which is applicable to K_3SeI absorber-based APSCs. This study demonstrates that carrier mobility is an important parameter in determining the performance of K_3SeI absorber-based solar cells. Fig. 16 shows that PCE, FF, and J_{SC} increase as the electron mobility increases, and PCE, FF, and J_{SC} decrease as the hole mobility increases. The exception is only for V_o, where V_o decreases as the electron mobility increases, and V_o increases as the hole mobility increases.

3.15. Impact of series and shunt resistance in the proposed solar cell device on the photovoltaic performance parameters (PCE, FF, J_{SC}, and V_O)

Series resistance (R_s) and shunt resistance (R_{sh}) play an important role in determining the performance of a solar cell. If the series resistance is high, the voltage drop across the device increases, which reduces the fill factor (FF) and power conversion efficiency (PCE). On the other hand, if the shunt resistance is low, the short-circuit current (J_{sc}) and overall efficiency decrease. At first, the study of how well K_3SeI absorber-based solar cells perform (like the JV and QE curves) and how to improve them, including factors like defect density, shallow acceptor density, and electron and hole mobility, here did not take into account the impact of series and shunt resistance, so it was mostly done. However, in real devices, R_s and R_{sh} are present, and they have a direct impact on voltage, current, and efficiency. Therefore, to maximize the performance of the K_3SeI absorber-based solar cell in SCAPS-1D, the photovoltaic parameters of the device were tested by varying R_s (0.2–2 $\Omega.cm^2$) and R_{sh} (10^2–10^6 $\Omega.cm^2$). The optimization results are presented in Fig. 17, which is applicable to K_3SeI absorber-based APSCs. This study shows that selecting appropriate series and shunt resistance significantly increases the efficiency and stability of solar cells, which provides important guidance for improving the design and performance of real devices. Therefore, we choose that the series resistance of 1.48 and shunt resistance of 10^6 $\Omega.cm^2$ yield the best photovoltaic results. This investigation of the series and shunt resistance of proposed solar cell device gave the best result, with a J_{sc} of 31.71 mA/cm^2, an FF of 82.88 %, a PCE of 29.84 %, and a V_o of 1.1355 V.

3.16. Comparative discussion of photovoltaic performance and material properties

Table 13 presents a comparative analysis of the photovoltaic performance of the proposed K_3SeI absorber-based anti-perovskite solar cell with previously reported high-efficiency perovskite and anti-perovskite devices. The K_3SeI-based device achieves a power conversion efficiency (PCE) of 29.84 %, with an open-circuit voltage (V_o) of 1.1355 V, a fill factor (FF) of 82.88 %, and a short-circuit current density (J_{SC}) of 29.84 mA/cm^2. These values are competitive with many reported lead-free and hybrid perovskite architectures. Although some previously reported devices exhibit slightly higher PCE values, such as CIGS/$MASnI_3$- and CsSn-based multi-absorber configurations, those structures often involve complex multilayer stacks or toxic/rare elements. In contrast, the Al/FTO/SnS_2/K_3SeI/CuO/Se architecture demonstrates a balanced

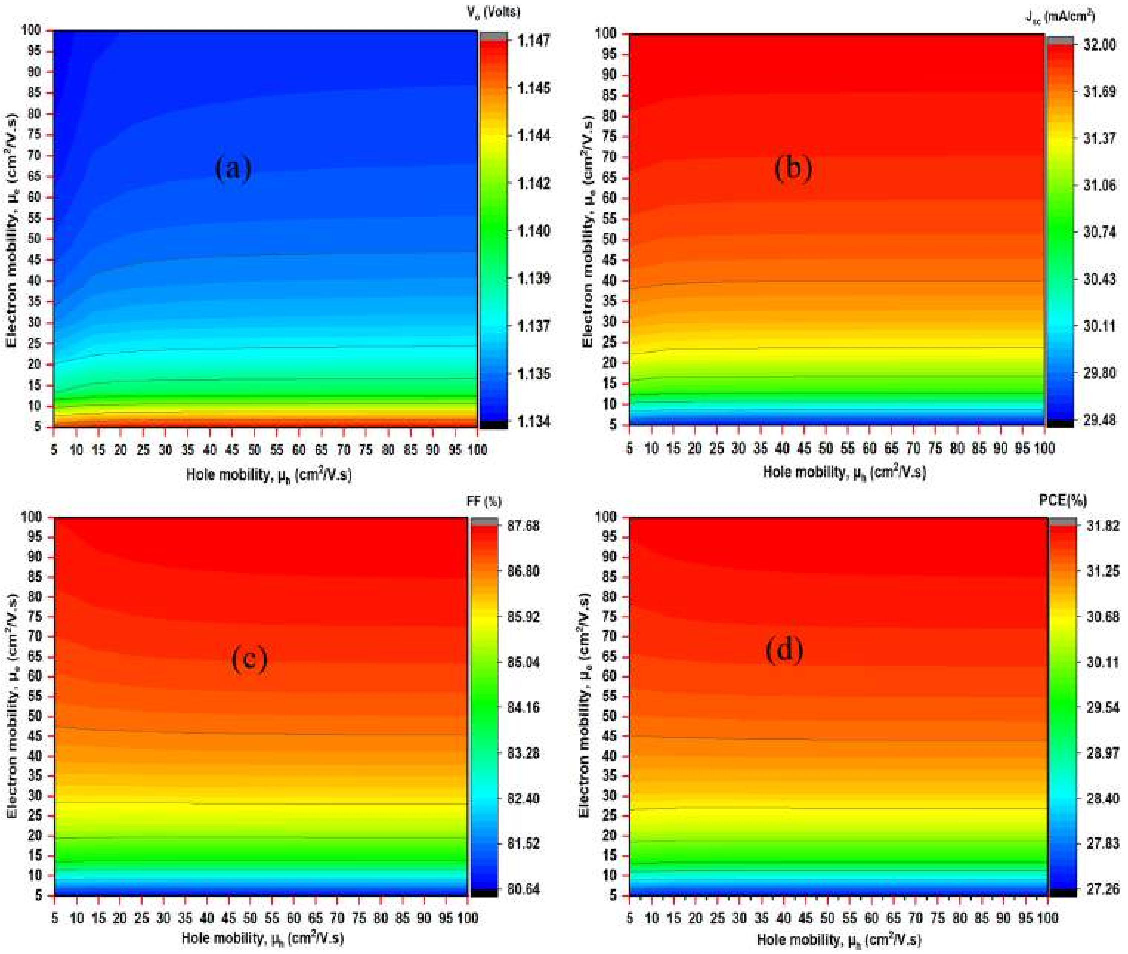

Fig. 16. Influence of electron and hole mobility in the K_3SeI absorber layer on (a) V_O, (b) J_{SC}, (c) FF, and (d) PCE of the proposed anti-perovskite solar cell.

photovoltaic response using a single active absorber layer with favorable band alignment and controlled interfacial recombination. When compared with structurally related anti-perovskite systems such as K_3SeBr and Na_3SBr, the K_3SeI device exhibits a higher PCE and improved current density, which can be attributed to its optimized bandgap, enhanced light absorption in the UV–visible region, and reduced interface recombination losses as confirmed by SCAPS-1D simulations. These results confirm that K_3SeI is a promising absorber material for high-performance, environmentally benign anti-perovskite solar cells.

Table 14 provides a comprehensive comparison of the dynamic, mechanical, and optoelectronic properties of K_3SeI with structurally and chemically similar perovskite and anti-perovskite systems. Compared to closely related compounds such as K_3OI, Na_3SI, and Na_3SBr, the bandgap of K_3SeI (1.7047 eV) lies within the optimal range for visible-light absorption and photovoltaic operation. The reduction in bandgap relative to Na_3SI and Na_3SBr can be attributed to the presence of heavier Se and I atoms, which enhance orbital overlap and reduce the energy separation between the valence and conduction bands. The electron and hole mobilities of K_3SeI are lower than those of Na_3SBr but remain sufficiently high for efficient charge transport. The observed reduction in mobility can be explained by the increased atomic mass of Se and I, which enhances electron–phonon scattering and slightly increases effective carrier mass. Nevertheless, the mobilities of K_3SeI remain superior to those of many conventional halide perovskites such as $MAPbI_3$ and $MASnI_3$, indicating its suitability for photovoltaic and optoelectronic applications. An unusually low static dielectric constant ($\varepsilon_1(0) = 2.064$) is observed for K_3SeI compared to conventional perovskites, where ε typically ranges from 10 to 30. This behavior is characteristic of inorganic anti-perovskites with reduced lattice polarizability. While a low dielectric constant may increase exciton binding energy, this effect is mitigated in K_3SeI by its strong light absorption coefficient, favorable band-edge alignment, and sufficient carrier mobility, enabling efficient exciton dissociation under operational conditions. Furthermore, K_3SeI demonstrates excellent phonon and mechanical stability, ensuring structural robustness under device operating conditions. The combined balance of optimized bandgap, strong absorption, acceptable carrier mobility, and favorable stability distinguishes K_3SeI from structurally similar anti-perovskites and supports its multifunctional applicability in photovoltaics, photocatalysis, and optoelectronic devices.

Although this work is entirely theoretical, earlier achievements within the anti-perovskite family indicate that K_3SeI could realistically be synthesized. For instance, sodium-based anti-perovskites such as Na_3OX (X = Cl, Br, I, BH_4) have been successfully produced and characterized through mechanochemical methods, demonstrating their practical feasibility [184]. Likewise, anti-perovskites of the Ca_3MN variety (M = As, P, Sb, Ge, Bi, Pb, Sn) have been experimentally realized, with their stability and reproducibility confirmed in laboratory settings [185]. The successful definition and synthesis of Mg_3AsN anti-perovskites further reinforce the likelihood of preparing similar compounds, including K_3SeI, in practice [186]. This evidence strongly suggests that K_3SeI is synthetically attainable, paving the way for future experimental exploration. Despite its excellent thermodynamic and mechanical stability supported by phonon analysis, elastic constants, and formation energy, one should consider that selenium and bromine possess some level of toxicity, and halide-containing materials may be prone to degradation under humid or ambient conditions. Therefore, careful encapsulation or protective coatings would be essential for

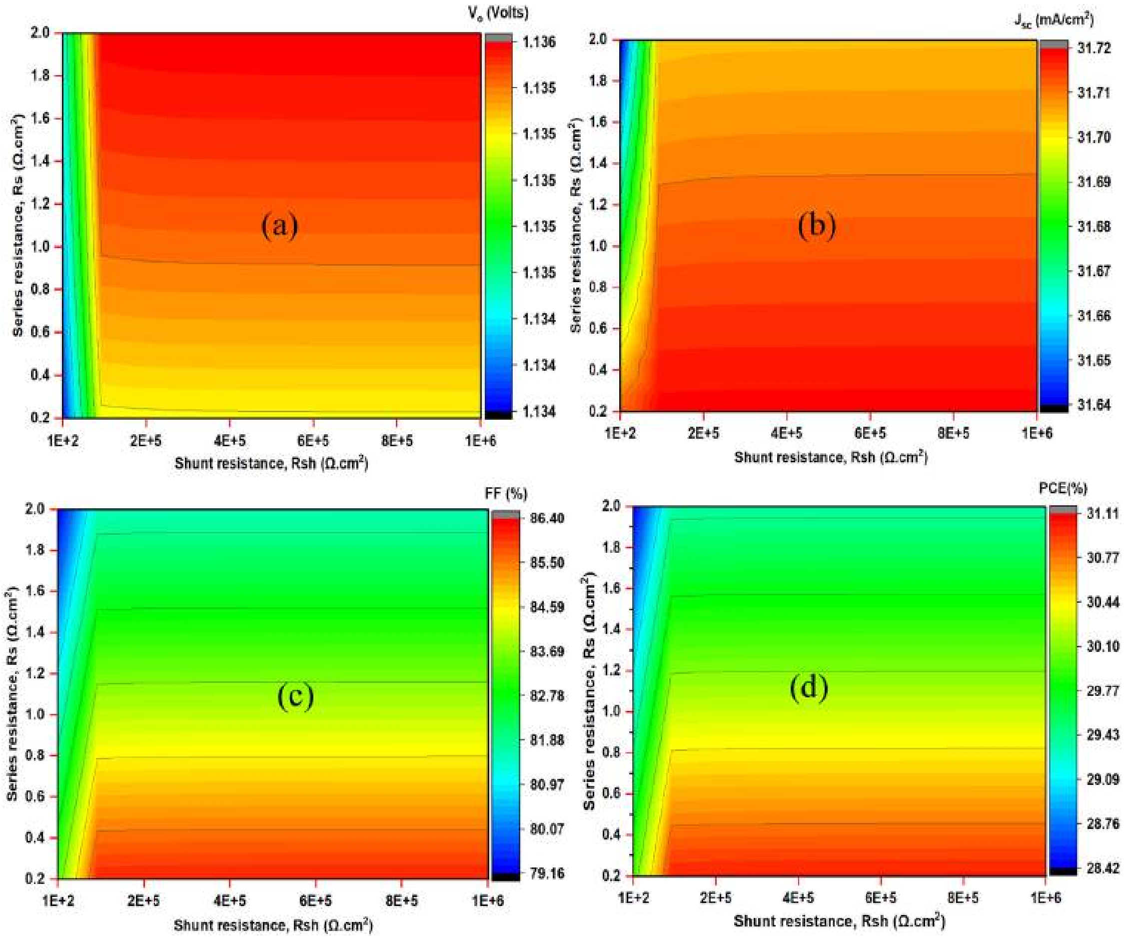

Fig. 17. Influence of series and shunt resistance in the proposed K_3SeI-absorber-layer-based solar cell device on (a) V_O, (b) J_{SC}, (c) FF, and (d) PCE.

Table 13
Comparison of photovoltaic performance of K_3SeI absorber APSC with earlier research findings.

Configuration	FF (%)	V_o (Volts)	PCE (%)	J_{sc} (mA/cm^2)	Reference
Au/Spiro-OmeTAD/CIGS/$MASnI_3$/CdS/ZnO/FTO	54.24	1.38	36.38	48.28	[175]
ITO/TiO_2/$NaZn_{0.7}Cu_{0.3}Br_3$/$MASnI_3$/CuO/ Au	82.19	1.1377	32.58	34.8389	[176]
SnS_2/$CsSn_{0.5}Ge_{0.5}I_3$/$FASnI_3$/Zn_3P_2/Pt	89.58	1.185	33.16	31.218	[177]
AZO/TiO_2/$CsPbI_3$/$RbGeI_3$/Ni	88.38	1.04	31.91	34.77	[178]
FTO/WO_3/$CsSnI_3$/$CsSnGeI_3$/$Cs_3Sb_2Br_9$/Cu_2O /Au	89.17	1.244	36.21	32.640	[179]
FTO/n + -$FASnI_3$/ETL/$FASnI_3$/HTL	87.33	1.1002	30.19	31.422	[180]
ITO/C_{60}/$MASnI_3$/$RbGeI_3$/Cu_2O/Au	65.49	0.914	32.7	20.19	[181]
ITO/ZnO/Cs_2BiAgI_6/CIGS/Spiro-OMeTAD/Au	85.01	1.108	31.89	30.10	[182]
Al/FTO/SnS_2/K_3SeI/CuO/Se	82.88	1.1355	29.84	31.71	**This work**
Al/FTO/SnS_2/K_3SeBr/CuO/Se	82	1.1648	28.02	29.363	[43]
Al/FTO/SnS_2/Na_3SBr/CuO/Au	84.51	1.544	27.172	20.82	[2]
FTO/SnS_2/CuAgBeSnSe$_4$/$FASnI_3$/CuO/Au	89.01	1.222	34.57	31.77	[183]

practical applications.

4. Conclusions

In this study, the structural, electronic, optical, photovoltaic, and photocatalytic properties of a novel anti-perovskite compound K_3SeI have been analyzed using DFT-based methods. The structure optimization, phonon dispersion, and elastic constant analysis showed that this compound is dynamically and mechanically stable, indicating the potential for its practical applications in the future. The analysis of electronic properties shows that K_3SeI is a direct bandgap added semiconductor with a bandgap of 1.7047 eV (GGA-PBE) and 2.5367 eV (HSE06) and is located at the gamma point. This bandgap value is essential for visible light absorption and energy conversion, especially in the case of photovoltaic and photocatalytic water splitting. The locations of the VBM and CVM edges of K_3SeI relatively match the redox potential of water splitting, suggesting that it is capable of efficiently producing hydrogen and oxygen in the presence of visible light. However, The (001) surface of K_3SeI anti-perovskite demonstrates remarkable thermodynamic stability, evidenced by its minimal surface energy of 0.000514 eV/Å^2. Adsorption research indicates that OH* and OOH* intermediates exhibit stronger binding than H* and O*, implying successful stabilization of critical reaction species on the surface. Free energy calculations reveal a minimal overpotential for hydrogen evolution (0.071 V), underscoring the surface's exceptional catalytic efficiency for HER, but a comparatively elevated overpotential for oxygen evolution

Table 14
Comparative analysis of the dynamic, mechanical, and optoelectronic properties of K_3SeI with previous studies.

Structure	$MAPBI_3$	$FASnI_3$	$MASnI_3$	K_3OI	Na_3SI	Na_3SBr	K_3SeBr	K_3SeI
Bandgap (eV)	1.55	4.2	1.3	1.03	2.499	2.5361	1.726	1.7047
Electron affinity (eV)	3.9	1.45	4.2	-	3.893	3.57	3.665	3.722
Dielectric constant, $\varepsilon_1(0)$	30	8.2	8.2	2.34	2.917	2.62	1.91	2.064
Light absorption capability (cm^{-1})	(1×10^5) visible region	(1×10^5) visible region	(1×10^5) visible region	(1.1×10^4) visible region	$(13 \times 10^5–0.5 \times 10^5)$ in the UV-to-visible region	$(13 \times 10^5–0.5 \times 10^5)$ in the UV-to-visible-to-NIR region	$(13 \times 10^5–0.5 \times 10^5)$ in the UV-to-visible-to-NIR region	$(6.8 \times 10^5–0.5 \times 10^5)$ in the UV-to-visible region
Mobility of electron, μ_e (cm^2/Vs)	2.2	22	1.6	-	63.18	55.16	38.7	42.2
Mobility of hole, μ_h (cm^2/Vs)	2.2	22	1.6	-	7.56	31.23	8.17	8.53
Phonon stability	Stable	Stable	Stable	Stable	Stable	Stable	Stable	Stable
Mechanical stability	Stable	Stable	Stable	Stable	Stable	Stable	Stable	Stable
Pugh's ratio	2.39 (ductile)	2.55 (ductile)	2.27 (ductile)	1.31 (brittle)	1.638 (brittle)	1.81 (ductile)	1.923 (ductile)	1.618 (brittle)
Application	Solar cell	Solar cell	Solar cell	Photo-catalysis, opto-electronic, and solar cell	Photo-catalysis, opto-electronic, and solar cell	Photo-catalysis, opto-electronic, and solar cell	Photo-catalysis, opto-electronic, and solar cell	Photovoltaic, Photo-catalysis, and opto-electronic
Reference	[187-189]	[190-192]	[193,194]	[64]	[1]	[2]	[43]	**This work**

(2.64 V) is noted. These results affirm that the (001) surface is structurally stable and catalytically active, establishing a robust basis for forthcoming experimental and surface-oriented applications. Also, the vacancy defect formation analysis of the 2 × 2 × 1 K_3SeI supercell shows that iodine vacancies are most easily formed, while potassium and selenium atoms are comparatively stable, providing key insights for defect engineering and material optimization. On the other hand, optical analysis of this compound also indicates that it exhibits a high absorption range from about $6.8 \times 10^5–0.5 \times 10^5$ cm^{-1} in the ultraviolet to visible light wavelength region. In addition, its medium-level dielectric constant, efficient optical absorption, low reflection coefficient, and high refraction in UV-to-visible light make it a potential material for future solar cells, light-sensing devices, and other optoelectronic applications. The SCAPS-1D simulations of the K_3SeI-based anti-perovskite solar cell demonstrate its strong potential as a high-efficiency absorber material. The optimized device structure, Al/FTO/SnS_2/K_3SeI/CuO/Se, exhibits excellent charge generation and low recombination throughout the 2 µm K_3SeI layer, supported by favorable energy band alignment and efficient carrier transport. The photovoltaic performance is remarkable, with a J_{SC} of 31.71 mA/cm^2, V_o of 1.1355 V, FF of 82.88 %, and PCE of 29.84 %. Device optimization shows that moderate defect density (10^{15} ($1/cm^3$)), proper shallow acceptor concentration (10^{15} ($1/cm^3$)), and balanced electron–hole mobility (42.2 and 8.53 $cm^2/V.s$) are crucial for maximizing efficiency, while appropriate series and shunt resistances (1.48 and 10^6 $\Omega.cm^2$) further enhance stability and output. Overall, these results confirm that K_3SeI is a promising absorber for high-performance inorganic anti-perovskite solar cells, comparable to other reported APSCs, and provides a solid foundation for future experimental implementation. However, as the current work relies entirely on first-principles theoretical analysis, its experimental synthesis and performance verification are essential in the future.

CRediT authorship contribution statement

Md. Earshad Ali: Data curation, Conceptualization, Formal analysis, Methodology, Investigation, Resources, Software, Validation, Visualization, Writing – original draft, Project administration, Writing – review and editing, Supervision. **Karim Kriaa:** Conceptualization, Formal analysis, Data curation, Investigation, Methodology, Software, Validation, Visualization, Writing – original draft, Writing – review and editing, Project administration, Funding acquisition**, Md. Nobiul Islam:** Investigation, Formal analysis, Resources, Software, Visualization, Methodology, Writing – original draft, Writing – review and editing, **Chemseddine Maatki:** Investigation, Validation, Software, Formal analysis, Data curation, Writing – original draft, Writing – review and editing**, Md. Shizer Rahman:** Formal analysis, Investigation, Supervision, Resources, Writing – review and editing, Software, Visualization, Writing – original draft**, Noureddine Elboughdiri:** Investigation, Validation, Software, Formal analysis, Data curation, Writing – original draft, Writing – review and editing**, Md. Azizur Rahman:** Investigation, Validation, Software, Formal analysis, Data curation, Writing – original draft, Writing – review and editing.

Ethical

The manuscript's authors agree that there is no research involving human participants, human data or tissue, or animal subjects.

Funding

This work was supported and funded by the Deanship of Scientific Research at Imam Mohammad Ibn Saud Islamic University (IMSIU) (grant number IMSIU-DDRSP2602).

Declaration of Competing Interest

The authors declare that they have no known competing financial interests or personal relationships that could have appeared to influence the work reported in this paper.

Acknowledgment

This work was supported and funded by the Deanship of Scientific Research at Imam Mohammad Ibn Saud Islamic University (IMSIU) (grant number IMSIU-DDRSP2602).

Data availability

Data will be made available on reasonable request.

References

[1] Md.E. Ali, First-principles investigation of the structural, electronic, and optical properties of a novel Na3SI anti-perovskite for efficient solar-to-hydrogen energy conversion via photocatalytic water splitting, Int. J. Hydrog. Energy 194 (Dec. 2025) 152217, https://doi.org/10.1016/j.ijhydene.2025.152217.

[2] Md.E. Ali, DFT-based investigation of optoelectronic, dynamic, thermodynamic, mechanical, and strain-engineered properties of a novel lead-free Na3SBr inorganic anti-perovskite and achieving over 27% solar cell efficiency, J Alloys Compd 1043 (2025) 184–221. https://doi.org/10.1016/j.jallcom.2025.184221.

[3] J.L. Young, K.X. Steirer, M.J. Dzara, J.A. Turner, T.G. Deutsch, Remarkable stability of unmodified GaAs photocathodes during hydrogen evolution in acidic electrolyte, J. Mater. Chem. A Mater. 4 (8) (2016) 2831–2836, https://doi.org/10.1039/C5TA07648J.

[4] J. Wu, T. Wu, Ensure access to affordable, reliable, sustainable and modern energy for all, UN Chron. 51 (4) (Jun. 2015) 17–18, https://doi.org/10.18356/24ef28d2-en.

[5] A. Rogalski, F. Wang, J. Wang, P. Martyniuk, W. Hu, The perovskite optoelectronic devices – a look at the future, Small Methods 9 (1) (Jan. 2025), https://doi.org/10.1002/smtd.202400709.

[6] Md.E. Ali, M.R. Islam, DFT-based investigation of thermal, dynamic, mechanical, optoelectronic, and strain-engineered properties of a novel lead-free Na3SeBr inorganic anti-perovskite compound and achieving over 29% photovoltaic efficiency, Mater. Today Commun. 51 (Feb. 2026) 114657, https://doi.org/10.1016/j.mtcomm.2026.114657.

[7] M.E. Ali, M.M. Haque, S.H. Cheragee, Device modeling and numerical analysis of lead-free MASnI3/Ca3AsI3 based perovskite solar cells with over 38% efficiency, Sol. Energy 288 (Mar. 2025), https://doi.org/10.1016/j.solener.2025.113309.

[8] G. Ji, et al., B-site columnar-ordered halide double perovskites: theoretical design and experimental verification, J. Am. Chem. Soc. 143 (27) (Jul. 2021) 10275–10281, https://doi.org/10.1021/jacs.1c03825.

[9] Z. Liu, et al., Bandgap engineering and thermodynamic stability of oxyhalide and chalcohalide antiperovskites, Ceram. Int 47 (23) (Dec. 2021) 32634–32640, https://doi.org/10.1016/j.ceramint.2021.08.159.

[10] H. Park, et al., Water splitting exceeding 17% solar-to-hydrogen conversion efficiency using solution-processed Ni-based electrocatalysts and perovskite/Si tandem solar cell, ACS Appl. Mater. Interfaces 11 (37) (Sep. 2019) 33835–33843, https://doi.org/10.1021/acsami.9b09344.

[11] O. Benguerine, Z. Nabi, A. Hachilif, B. Bouabdallah, B. Benichou, Bright future in optoelectronics, photovoltaics and thermoelectric using the double perovskites oxides BaSrMgB'O6 (B'=Te, W), Comput. Condens. Matter 30 (Mar. 2022) e00649, https://doi.org/10.1016/j.cocom.2022.e00649.

[12] X. Li, Y. Zhang, W. Kang, Z. Yan, Y. Shen, J. Huo, Anti-perovskite nitrides and oxides: properties and preparation, Comput. Mater. Sci. 225 (Jun. 2023) 112188, https://doi.org/10.1016/j.commatsci.2023.112188.

[13] Y. Wang, et al., Antiperovskites with exceptional functionalities, Adv. Mater. 32 (7) (Feb. 2020), https://doi.org/10.1002/adma.201905007.

[14] M.Y. Chern, D.A. Vennos, F.J. Disalvo, Synthesis, structure, and properties of anti-perovskite nitrides Ca3MN, M=P, As, Sb, Bi, Ge, Sn, and Pb, J. Solid State Chem. 96 (2) (Feb. 1992) 415–425, https://doi.org/10.1016/S0022-4596(05)80276-2.

[15] G. Tang, et al., Designing antiperovskite derivatives *via* atomic-position splitting for photovoltaic applications, Mater. Horiz. 11 (21) (2024) 5320–5330, https://doi.org/10.1039/D4MH00526K.

[16] H. Zhong, et al., Structure–composition–property relationships in antiperovskite nitrides: guiding a rational alloy design, ACS Appl. Mater. Interfaces 13 (41) (Oct. 2021) 48516–48524, https://doi.org/10.1021/acsami.1c10137.

[17] D. Kalita, P. Sahu, U. Manju, Anti-perovskites for photovoltaics: materials development and challenges, J. Phys. D. Appl. Phys. 57 (34) (Aug. 2024) 343002, https://doi.org/10.1088/1361-6463/ad4daf.

[18] S.A. Khandy, I. Islam, A. Laref, M. Gogolin, A.K. Hafiz, A.M. Siddiqui, Electronic structure, thermomechanical and phonon properties of inverse perovskite oxide (Na3OCl): an ab initio study, Int. J. Energy Res 44 (4) (Mar. 2020) 2594–2603, https://doi.org/10.1002/er.4982.

[19] K.T. Lai, I. Antonyshyn, Y. Prots, M. Valldor, *Anti* -perovskite Li-battery cathode materials, J. Am. Chem. Soc. 139 (28) (Jul. 2017) 9645–9649, https://doi.org/10.1021/jacs.7b04444.

[20] G.S.H. Thien, et al., Recent advances in halide perovskite resistive switching memory devices: a transformation from lead-based to lead-free perovskites, ACS Omega 7 (44) (Nov. 2022) 39472–39481, https://doi.org/10.1021/acsomega.2c03206.

[21] U. Rani, et al., Electronic structure, theoretical power conversion efficiency, and thermoelectric properties of bismuth-based alkaline earth antiperovskites, J. Mol. Model 29 (10) (Oct. 2023) 329, https://doi.org/10.1007/s00894-023-05732-z.

[22] A. Meziany, et al., Toward lightweight solid-state hydrogen storage: computational investigation of potassium antiperovskites, Phys. Status Solidi (a) (Jun. 2025), https://doi.org/10.1002/pssa.202500168.

[23] S. Liu, et al., Efficient photocatalytic hydrogen evolution over carbon supported antiperovskite cobalt zinc nitride, Chem. Eng. J. 408 (Mar. 2021) 127307, https://doi.org/10.1016/j.cej.2020.127307.

[24] F. Zheng, M. Kotobuki, S. Song, M.O. Lai, L. Lu, Review on solid electrolytes for all-solid-state lithium-ion batteries, J. Power Sources 389 (Jun. 2018) 198–213, https://doi.org/10.1016/j.jpowsour.2018.04.022.

[25] X. Lü, et al., Antiperovskite Li$_3$OCl superionic conductor films for solid-state li-ion batteries, Adv. Sci. 3 (3) (Mar. 2016), https://doi.org/10.1002/advs.201500359.

[26] S. Nishioka, F.E. Osterloh, X. Wang, T.E. Mallouk, K. Maeda, Photocatalytic water splitting, Nat. Rev. Methods Prim. 3 (1) (Jun. 2023) 42, https://doi.org/10.1038/s43586-023-00226-x.

[27] C. Kang, S. Lian, C. Li, J. Ren, M. Chen, Micro-mechanism investigation of hydrogen evolution reaction on anti-perovskite Ni3InN considering doping and strain effects, Appl. Surf. Sci. 652 (Apr. 2024) 159366, https://doi.org/10.1016/j.apsusc.2024.159366.

[28] H.-X. Gao, et al., First-principles study on the structural, electronic, elastic, optical and thermodynamic properties of double antiperovskites X6BiSbN2 (X = Mg, Ca, Sr), J. Phys. Chem. Solids 187 (Apr. 2024) 111859, https://doi.org/10.1016/j.jpcs.2023.111859.

[29] T. Zafer, F. Kurtuluş, R. Salimov, E. Karaca, Investigation of the physical and superconductivity properties of Ni3AC (A = Mg, Zn and Cd), Solid State Commun. 397 (Mar. 2025) 115802, https://doi.org/10.1016/j.ssc.2024.115802.

[30] T. Hu, et al., Thermoelectric properties of lead-free anti-perovskites X3BN (B = Bi, Sb, X = Mg, Ca, Sr): A theoretical study based on first-principles calculations and machine learning interatomic potential, AIP Adv. 14 (4) (Apr. 2024), https://doi.org/10.1063/5.0201601.

[31] A.L. Bédé, et al., Theoretical study by density functional theory method (DFT) of stability, tautomerism, reactivity and prediction of acidity of quinolein-4-one derivatives, Comput. Chem. 06 (03) (2018) 57–70, https://doi.org/10.4236/cc.2018.63005.

[32] J.P. Perdew, A. Zunger, Self-interaction correction to density-functional approximations for many-electron systems, Phys. Rev. B 23 (10) (May 1981) 5048–5079, https://doi.org/10.1103/PhysRevB.23.5048.

[33] P. Giannozzi, et al., QUANTUM ESPRESSO: a modular and open-source software project for quantum simulations of materials, J. Phys. Condens. Matter 21 (39) (Sep. 2009) 395502, https://doi.org/10.1088/0953-8984/21/39/395502.

[34] G. Kresse, J. Hafner, Norm-conserving and ultrasoft pseudopotentials for first-row and transition elements, J. Phys. Condens. Matter 6 (40) (Oct. 1994) 8245–8257, https://doi.org/10.1088/0953-8984/6/40/015.

[35] P. Haas, F. Tran, P. Blaha, K. Schwarz, Construction of an optimal GGA functional for molecules and solids, Phys. Rev. B 83 (20) (May 2011) 205117, https://doi.org/10.1103/PhysRevB.83.205117.

[36] Z. Wu, R.E. Cohen, More accurate generalized gradient approximation for solids, Phys. Rev. B 73 (23) (Jun. 2006) 235116, https://doi.org/10.1103/PhysRevB.73.235116.

[37] P. Giannozzi, et al., Advanced capabilities for materials modelling with Quantum ESPRESSO, J. Phys. Condens. Matter 29 (46) (Nov. 2017) 465901, https://doi.org/10.1088/1361-648X/aa8f79.

[38] H.S. Patel, V.A. Dabhi, A.M. Vora, Adverse effect of K-Mesh shifting in several crystal Systems: An analytical study, Mater. Today Proc. 57 (2022) 275–278, https://doi.org/10.1016/j.matpr.2022.02.599.

[39] D.R. Hamann, M. Schlüter, C. Chiang, Norm-Conserving Pseudopotentials, Phys. Rev. Lett. 43 (20) (Nov. 1979) 1494–1497, https://doi.org/10.1103/PhysRevLett.43.1494.

[40] F. Karsch, A. Patkós, P. Petreczky, Screened perturbation theory, Phys. Lett. B 401 (1–2) (May 1997) 69–73, https://doi.org/10.1016/S0370-2693(97)00392-4.

[41] A.A. Aloufi, Z.A. Alahmed, A. Laref, H.A. Albrithen, Strain effects on structural, electronic, and optical properties of BeO by DFT, Mater. Res Bull. 114 (Jun. 2019) 52–60, https://doi.org/10.1016/j.materresbull.2019.02.015.

[42] S. Kahlaoui, B. Belhorma, H. Labrim, M. Boujnah, M. Regragui, Strain effects on the electronic, optical and electrical properties of Cu2ZnSnS4: DFT study, Heliyon 6 (4) (Apr. 2020) e03713, https://doi.org/10.1016/j.heliyon.2020.e03713.

[43] Md.E. Ali, et al., First-principles investigation of the structural, dynamic, mechanical, and optoelectronic features of novel K3SeBr anti-perovskite for photovoltaic and photocatalytic water splitting (solar-to-hydrogen production), J. Alloy. Compd. 1053 (Feb. 2026) 186163, https://doi.org/10.1016/j.jallcom.2026.186163.

[44] B. Huang, Y. Liu, Y. Zhang, F. Zhang, Y. Yang, J. Li, Effect of Vacancy Defects on the Electronic Structure and Optical Properties of Bi4O5Br2: First-Principles Calculations, Coatings 14 (11) (Oct. 2024) 1361, https://doi.org/10.3390/coatings14111361.

[45] X. Yong, A. Wang, L. Deng, X. Zhou, J. Li, Effects of vacancy defects on electrical and optical properties of ZnO/WSe2 heterostructure: first-principles study, Metals 12 (11) (Nov. 2022) 1975, https://doi.org/10.3390/met12111975.

[46] B. Baldassarri, et al., Accuracy of DFT computed oxygen-vacancy formation energies and high-throughput search of solar thermochemical water-splitting compounds, Phys. Rev. Mater. 7 (6) (Jun. 2023) 065403, https://doi.org/10.1103/PhysRevMaterials.7.065403.

[47] S. Ali, T. Liu, Z. Lian, D. Sheng Su, B. Li, The stability and reactivity of transition metal atoms supported mono and di vacancies defected carbon based materials revealed from first principles study, Appl. Surf. Sci. 473 (Apr. 2019) 777–784, https://doi.org/10.1016/j.apsusc.2018.12.153.

[48] P.M. Ismail, et al., Stable and robust single transition metal atom catalyst for CO2 reduction supported on defective WS2, Appl. Surf. Sci. 624 (Jul. 2023) 157073, https://doi.org/10.1016/j.apsusc.2023.157073.

[49] R. Jacobs, J. Booske, D. Morgan, Understanding and controlling the work function of perovskite oxides using density functional theory, Adv. Funct. Mater. 26 (30) (Aug. 2016) 5471–5482, https://doi.org/10.1002/adfm.201600243.

[50] T. Ma, R. Jacobs, J. Booske, D. Morgan, Discovery and engineering of low work function perovskite materials, J. Mater. Chem. C. Mater. 9 (37) (2021) 12778–12790, https://doi.org/10.1039/D1TC01286J.

[51] X. Feng, et al., Linear regulation of perovskite work function through organic molecular layer surface modification, Appl. Phys. Lett. 126 (14) (Apr. 2025), https://doi.org/10.1063/5.0253275.

[52] M. Ezzeldien, et al., Electronic and optical properties of bulk and surface of CsPbBr3 inorganic halide perovskite a first principles DFT 1/2 approach, Sci. Rep. 11 (1) (Oct. 2021) 20622, https://doi.org/10.1038/s41598-021-99551-y.

[53] L. Ge, et al., Predicted optimal bifunctional electrocatalysts for the hydrogen evolution reaction and the oxygen evolution reaction using chalcogenide heterostructures based on machine learning analysis of in silico quantum mechanics based high throughput screening, J. Phys. Chem. Lett. 11 (3) (Feb. 2020) 869–876, https://doi.org/10.1021/acs.jpclett.9b03875.

[54] S. Kosasang, et al., Insight into the effect of intercalated alkaline cations of layered manganese oxides on the oxygen reduction reaction and oxygen evolution reaction, Chem. Commun. 54 (62) (2018) 8575–8578, https://doi.org/10.1039/C8CC03775B.

[55] V. Yadav, Megha P. Sen, M.M. Shaijumon, Electrosynthesis of ruthenium nanocluster incorporated nickel diselenide for efficient overall water splitting, J. Mater. Chem. A Mater. 12 (9) (2024) 5319–5330, https://doi.org/10.1039/D3TA06988E.

[56] F. Zhou, P. Yu‡, F. Sun, G. Zhang, X. Liu, L. Wang, The cooperation of Fe_3C nanoparticles with isolated single iron atoms to boost the oxygen reduction reaction for Zn–air batteries, J. Mater. Chem. A Mater. 9 (11) (2021) 6831–6840, https://doi.org/10.1039/D1TA00039J.

[57] P.M. Ismail, et al., Photoelectron 'Bridge' in Van Der Waals Heterojunction for Enhanced Photocatalytic CO_2 Conversion Under Visible Light, Adv. Mater. 35 (38) (Sep. 2023), https://doi.org/10.1002/adma.202303047.

[58] L. Bao, et al., Modulating the doping state of transition metal ions in ZnS for enhanced photocatalytic activity, Chem. Commun. 59 (75) (2023) 11280–11283, https://doi.org/10.1039/D3CC03436D.

[59] K. Deepthi Jayan, V. Sebastian, Comprehensive device modelling and performance analysis of MASnI3 based perovskite solar cells with diverse ETM, HTM and back metal contacts, Sol. Energy 217 (Mar. 2021) 40–48, https://doi.org/10.1016/j.solener.2021.01.058.

[60] S. Karthick, S. Velumani, J. Bouclé, Chalcogenide BaZrS3 perovskite solar cells: A numerical simulation and analysis using SCAPS-1D, Opt. Mater. (Amst.) 126 (Apr. 2022), https://doi.org/10.1016/j.optmat.2022.112250.

[61] M. Burgelman, K. Decock, S. Khelifi, A. Abass, Advanced electrical simulation of thin film solar cells, Thin Solid Films 535 (May 2013) 296–301, https://doi.org/10.1016/j.tsf.2012.10.032.

[62] Y. Wang, S. J Laihonen, M. Unge, A.A. Mostofi, Improving the precision of work-function calculations within plane-wave density functional theory, Electron. Struct. 6 (3) (Sep. 2024) 037004, https://doi.org/10.1088/2516-1075/ad72c2.

[63] H. Abedini-Ahangarkola, S. SoleimaniAmiri, S. Gholami Rudi, Modeling and numerical simulation of high efficiency perovskite solar cell with three active layers, Sol. Energy 236 (Apr. 2022) 724–732, https://doi.org/10.1016/j.solener.2022.03.055.

[64] Q.-Q. Liang, et al., First-principles calculations to investigate structural, electronic, optical and thermodynamic properties of anti-perovskite compounds X3OI(X = Na, K, Rb), J. Mater. Res. Technol. 22 (Jan. 2023) 3245–3254, https://doi.org/10.1016/j.jmrt.2022.12.148.

[65] Z. Lv, H. Cui, H. Wang, X. Li, G. Ji, Electronic, elastic, lattice dynamic and thermal conductivity properties of Na 3 OBr via first principles, Phys. Status Solidi (b) 254 (9) (Sep. 2017), https://doi.org/10.1002/pssb.201700089.

[66] S.A. Khandy, I. Islam, A. Laref, M. Gogolin, A.K. Hafiz, A.M. Siddiqui, Electronic structure, thermomechanical and phonon properties of inverse perovskite oxide (Na 3 OCl): An ab initio study, Int J. Energy Res 44 (4) (Mar. 2020) 2594–2603, https://doi.org/10.1002/er.4982.

[67] A. Togo, I. Tanaka, First principles phonon calculations in materials science, Scr. Mater. 108 (Nov. 2015) 1–5, https://doi.org/10.1016/j.scriptamat.2015.07.021.

[68] M. Hong, et al., Realizing zT of 2.3 in Ge $1- x - y$ Sb x In y Te via Reducing the Phase-Transition Temperature and Introducing Resonant Energy Doping, Adv. Mater. 30 (11) (Mar. 2018), https://doi.org/10.1002/adma.201705942.

[69] A.S. Oreshonkov, E.M. Roginskii, V.V. Atuchin, New candidate to reach Shockley–Queisser limit: The DFT study of orthorhombic silicon allotrope Si (oP32), J. Phys. Chem. Solids 137 (Feb. 2020) 109219, https://doi.org/10.1016/j.jpcs.2019.109219.

[70] Y.N. Zhuravlev, V.V. Atuchin, Comprehensive Density Functional Theory Studies of Vibrational Spectra of Carbonates, Nanomaterials 10 (11) (Nov. 2020) 2275, https://doi.org/10.3390/nano10112275.

[71] Y.G. Denisenko, et al., Crystal Structure, Vibrational, Spectroscopic and Thermochemical Properties of Double Sulfate Crystalline Hydrate [CsEu(H2O)3(SO4)2]·H2O and Its Thermal Dehydration Product CsEu(SO4)2, Cryst. (Basel) 11 (9) (Aug. 2021) 1027, https://doi.org/10.3390/cryst11091027.

[72] A. Sharma, P. Suryanarayana, Calculation of phonons in real-space density functional theory, Phys. Rev. E 108 (4) (Oct. 2023) 045302, https://doi.org/10.1103/PhysRevE.108.045302.

[73] E. Mohebbi, E. Pavoni, D. Mencarelli, P. Stipa, E. Laudadio, L. Pierantoni, Stability, phonon calculations, electronic structure, and optical properties of a VO2(M) nanostructure: A comprehensive density functional theory study, Front Mater. 10 (Feb. 2023), https://doi.org/10.3389/fmats.2023.1145822.

[74] W. Sun, L. Li, J. Zhang, H. Yin, Theoretical Study of Phonon Dispersion of Lanthanum Aluminate in Terahertz Frequency, Procedia Comput. Sci. 147 (2019) 90–96, https://doi.org/10.1016/j.procs.2019.01.196.

[75] Y.N. Zhuravlev, V.V. Atuchin, First-Principle Studies of the Vibrational Properties of Carbonates under Pressure, Sensors 21 (11) (May 2021) 3644, https://doi.org/10.3390/s21113644.

[76] Y. Zhuravlev, V. Atuchin, Chemical Bonding Effects and Physical Properties of Noncentrosymmetric Hexagonal Fluorocarbonates ABCO3F (A: K, Rb, Cs; B: Mg, Ca, Sr, Zn, Cd), Molecules 27 (20) (Oct. 2022) 6840, https://doi.org/10.3390/molecules27206840.

[77] F. Mouhat, F.-X. Coudert, Necessary and sufficient elastic stability conditions in various crystal systems, Phys. Rev. B 90 (22) (Dec. 2014) 224104, https://doi.org/10.1103/PhysRevB.90.224104.

[78] N. Erum, J. Ahmad, Structural, Elastic and Mechanical Properties of Cubic Perovskite Materials, Arch. Adv. Eng. Sci. 2 (1) (Jun. 2023) 24–29, https://doi.org/10.47852/bonviewAAES3202944.

[79] B. Rehmat, M.A. Rafiq, Y. Javed, Z. Irshad, N. Ahmed, S.M. Mirza, Elastic properties of perovskite-type hydrides LiBeH3 and NaBeH3 for hydrogen storage, Int J. Hydrog. Energy 42 (15) (Apr. 2017) 10038–10046, https://doi.org/10.1016/j.ijhydene.2017.01.109.

[80] M.I. Naher, M.A. Afzal, S.H. Naqib, A comprehensive DFT based insights into the physical properties of tetragonal superconducting Mo5PB2, Results Phys. 28 (Sep. 2021) 104612, https://doi.org/10.1016/j.rinp.2021.104612.

[81] M.E. Eberhart, T.E. Jones, Cauchy pressure and the generalized bonding model for nonmagnetic bcc transition metals, Phys. Rev. B 86 (13) (Oct. 2012) 134106, https://doi.org/10.1103/PhysRevB.86.134106.

[82] M.I. Naher, S.H. Naqib, An ab-initio study on structural, elastic, electronic, bonding, thermal, and optical properties of topological Weyl semimetal TaX (X = P, As), Sci. Rep. 11 (1) (Mar. 2021) 5592, https://doi.org/10.1038/s41598-021-85074-z.

[83] O.N. Senkov, D.B. Miracle, Generalization of intrinsic ductile-to-brittle criteria by Pugh and Pettifor for materials with a cubic crystal structure, Sci. Rep. 11 (1) (Feb. 2021) 4531, https://doi.org/10.1038/s41598-021-83953-z.

[84] S. Daoud, Sound velocities and Debye temperature of BeSe under high pressure up to 50 GPa, Int. J. Phys. Res. 5 (1) (Dec. 2016) 7–10, https://doi.org/10.14419/ijpr.v5i1.7013.

[85] P. Kuchhal, N. Dass, A New Model to Study the Sound Velocity in Liquid Metals, 1, Gazi Univ. J. Sci. (Jul. 2025) 1, https://doi.org/10.35378/gujs.1502124.

[86] S. Speziale, S.R. Shieh, T.S. Duffy, High-pressure elasticity of calcium oxide: A comparison between Brillouin spectroscopy and radial X-ray diffraction, J. Geophys Res Solid Earth 111 (B2) (Feb. 2006), https://doi.org/10.1029/2005JB003823.

[87] X. Du, D. He, H. Mei, Y. Zhong, N. Cheng, Insights on electronic structures, elastic features and optical properties of mixed-valence double perovskites Cs2Au2X6 (X=F, Cl, Br, I), Phys. Lett. A 384 (8) (Mar. 2020) 126169, https://doi.org/10.1016/j.physleta.2019.126169.

[88] Y. Liu, X. Zhang, H. Bi, X. Liu, F. Wang, First-principles prediction of structure, mechanical and thermodynamic properties of BixGeyOz ternary bismuth crystals, Vacuum 195 (Jan. 2022) 110696, https://doi.org/10.1016/j.vacuum.2021.110696.

[89] D.-Y. Hu, et al., First-principles calculations to investigate the structural, electronic and optical properties of lead-free double perovskites Rb2SeI6 and K2SeI6, Sol. Energy 231 (Jan. 2022) 236–242, https://doi.org/10.1016/j.solener.2021.11.062.

[90] X. Shi, et al., Highly Efficient ultra-thin solar selective absorber based on Self-assembled tangent Nano-Ball-Cap arrays, Chem. Eng. J. 505 (Feb. 2025) 159459, https://doi.org/10.1016/j.cej.2025.159459.

[91] Md.F. Rahman, et al., The optical and electronic properties of inorganic halide perovskite Sr3NCl3 under applied biaxial strain, J. Mater. Sci. 58 (32) (Aug. 2023) 13100–13117, https://doi.org/10.1007/s10853-023-08825-5.

[92] A. Ghosh, et al., Inorganic novel cubic halide perovskite Sr3AsI3: Strain-activated electronic and optical properties, Heliyon 9 (8) (Aug. 2023) e19271, https://doi.org/10.1016/j.heliyon.2023.e19271.

[93] Md.F. Rahman, et al., Unraveling the strain-induced and spin–orbit coupling effect of novel inorganic halide perovskites of Ca3AsI3 using DFT, AIP Adv. 13 (8) (Aug. 2023), https://doi.org/10.1063/5.0156961.

[94] A. Dubavik, V. Lesnyak, N. Gaponik, A. Eychmüller, A versatile approach for a variety of amphiphilic nanoparticles: semiconductor – plasmonic – magnetic, Z. F. üR. Phys. Chem. 228 (2–3) (Mar. 2014) 171–181, https://doi.org/10.1515/zpch-2014-0474.

[95] V.V. Atuchin, et al., Flux Crystal Growth and the Electronic Structure of $BaFe_{12}O_{19}$ Hexaferrite, J. Phys. Chem. C. 120 (9) (Mar. 2016) 5114–5123, https://doi.org/10.1021/acs.jpcc.5b12243.

[96] A.H. Reshak, et al., Exploration of the electronic structure of monoclinic α-$Eu_2(MoO_4)_3$: DFT-based study and X-ray photoelectron spectroscopy, J. Phys. Chem. C. 120 (19) (May 2016) 10559–10568, https://doi.org/10.1021/acs.jpcc.6b01489.

[97] A. Ghosh, et al., Investigating of novel inorganic cubic perovskites of A3BX3 (A=Ca, Sr, B P, As, X=I, Br) and their photovoltaic performance with efficiency

over 28, J. Alloy. Compd. 986 (May 2024) 174097, https://doi.org/10.1016/j.jallcom.2024.174097.

[98] J.O. Vasseur, P.A. Deymier, L. Dobrzynski, J. Choi, Electronic band gaps in one-dimensional comb structures of simple metals, J. Phys. Condens. Matter 10 (40) (Oct. 1998) 8973–8981, https://doi.org/10.1088/0953-8984/10/40/005.

[99] L. Huang, Z. Chen, J. Li, Effects of strain on the band gap and effective mass in two-dimensional monolayer GaX (X = S, Se, Te), RSC Adv. 5 (8) (2015) 5788–5794, https://doi.org/10.1039/C4RA12107D.

[100] S. Tariq, L.H. Omari, F. Mezzat, E.K. Hlil, Investigation of structural, electronic, optical, and photocatalytic properties of new double perovskites Cs2InSbX6 (X = F, Cl) under strain effects, Heliyon 10 (22) (Nov. 2024) e40315, https://doi.org/10.1016/j.heliyon.2024.e40315.

[101] J. Wei, Y. Guo, G. Wang, Effects of isotropic strain on the structure and transport properties of half-Heusler alloy BiBaK: a first-principles investigation, RSC Adv. 14 (1) (2024) 463–477, https://doi.org/10.1039/D3RA07345A.

[102] C.-H. Ri, Y.-S. Kim, U.-G. Jong, Y.-H. Kye, S.-H. Ryang, C.-J. Yu, First-principles study on structural, electronic and optical properties of perovskite solid solutions KB 1−x Mg x I 3 (B = Ge, Sn) toward water splitting photocatalysis, RSC Adv. 11 (42) (2021) 26432–26443, https://doi.org/10.1039/D1RA04534B.

[103] J. Xu, W. Wang, S. Sun, L. Wang, Enhancing visible-light-induced photocatalytic activity by coupling with wide-band-gap semiconductor: a case study on Bi2WO6/TiO2, 112, Appl. Catal. B 111 (Jan. 2012) 126–132, https://doi.org/10.1016/j.apcatb.2011.09.025.

[104] S. Saleem, et al., A band gap engineering for the modification in electrical properties of Fe3O4 by Cu2+ doping for electronic and optoelectronic devices applications, J. Solgel Sci. Technol. 109 (2) (Feb. 2024) 471–482, https://doi.org/10.1007/s10971-023-06287-4.

[105] M. Kumar, S. Rani, Y. Singh, K.S. Gour, V.N. Singh, Tin-selenide as a futuristic material: properties and applications, RSC Adv. 11 (12) (2021) 6477–6503, https://doi.org/10.1039/D0RA09807H.

[106] Y. Gu, J.P. Romankiewicz, J.K. David, J.L. Lensch, L.J. Lauhon, Quantitative measurement of the electron and hole mobility−lifetime products in semiconductor nanowires, Nano Lett. 6 (5) (May 2006) 948–952, https://doi.org/10.1021/nl052576y.

[107] S. Mamoun, A.E. Merad, New eco-friendly Rb2PtI6 based double perovskite solar cells with high photovoltaic performance up to 26% efficiency: numerical simulation, Renew. Energy 240 (Feb. 2025) 122268, https://doi.org/10.1016/j.renene.2024.122268.

[108] E.R. Burmistrov, L.P. Avakyants, M.M. Afanasova, Piezoelectric Relaxation of Two-Dimensional Electron Gas in Heterostructures with InGaN/GaN Quantum Wells, Russ. Phys. J. 64 (5) (Sep. 2021) 770–782, https://doi.org/10.1007/s11182-021-02391-6.

[109] D.M. Caughey, R.E. Thomas, "Carrier mobilities in silicon empirically related to doping and field, Proc. IEEE 55 (12) (1967) 2192–2193, https://doi.org/10.1109/PROC.1967.6123.

[110] W. Liu, X. Yan, G. Chen, Z. Ren, "Recent advances in thermoelectric nanocomposites, Nano Energy 1 (1) (Jan. 2012) 42–56, https://doi.org/10.1016/J.NANOEN.2011.10.001.

[111] Brennan and K. F., The Physics of Semiconductors. 1999. Accessed: Jun. 12, 2025, (Online). Available: 〈https://ui.adsabs.harvard.edu/abs/1999phse.book……B/abstract〉.

[112] C. Zhang, R. Wang, H. Mishra, Y. Liu, 2023, Two-Dimensional Semiconductors with High Intrinsic Carrier Mobility at Room Temperature," 2023, https://doi.org/10.1103/PhysRevLett.130.087001.

[113] S.H. Mir, V.K. Yadav, J.K. Singh, J.K. Singh, "Recent advances in the carrier mobility of two-dimensional materials: a theoretical perspective, ACS Omega 5 (24) (Jun. 2020) 14203–14211, https://doi.org/10.1021/ACSOMEGA.0C01676/ASSET/IMAGES/LARGE/AO0C01676_0003.JPEG.

[114] L. Cheng, C. Zhang, Y. Liu, "Intrinsic charge carrier mobility of 2D semiconductors, Comput. Mater. Sci. 194 (Jun. 2021) 110468, https://doi.org/10.1016/J.COMMATSCI.2021.110468.

[115] Y. Zhai, et al., Individual Electron and Hole Mobilities in Lead-Halide Perovskites Revealed by Noncontact Methods, ACS Energy Lett. 5 (1) (Jan. 2020) 47–55, https://doi.org/10.1021/acsenergylett.9b02310.

[116] M.T. Ilyas, K. Kaur, J. Sharma, G.S.S. Saini, DFT study of electronic structure and mobility of pristine and fluorinated methylammonium lead halide perovskites (CH 3 NH 3 PbX 3, X = I, Br, Cl), Int J. Energy Res 46 (5) (Apr. 2022) 6889–6900, https://doi.org/10.1002/er.7623.

[117] J. Lim, et al., Long-range charge carrier mobility in metal halide perovskite thin-films and single crystals via transient photo-conductivity, Nat. Commun. 13 (1) (Jul. 2022) 4201, https://doi.org/10.1038/s41467-022-31569-w.

[118] Z. Zhang, B. Saparov, Charge carrier mobility of halide perovskite single crystals for ionizing radiation detection, Appl. Phys. Lett. 119 (3) (Jul. 2021), https://doi.org/10.1063/5.0057411.

[119] P.K. Nayak, N. Periasamy, Calculation of electron affinity, ionization potential, transport gap, optical band gap and exciton binding energy of organic solids using 'solvation' model and DFT, Org. Electron 10 (7) (Nov. 2009) 1396–1400, https://doi.org/10.1016/j.orgel.2009.06.011.

[120] L. Lin, R. Jacobs, T. Ma, D. Chen, J. Booske, D. Morgan, Work Function: Fundamentals, Measurement, Calculation, Engineering, and Applications, Phys. Rev. Appl. 19 (3) (Mar. 2023) 037001, https://doi.org/10.1103/PhysRevApplied.19.037001.

[121] C. Kaewmeechai, Y. Laosiritaworn, A.P. Jaroenjittichai, Band alignment of Cs2BX6 double halide perovskites and TiO2 using electron affinity rule, Results Phys. 42 (Nov. 2022) 106015, https://doi.org/10.1016/j.rinp.2022.106015.

[122] S. Kashiwaya, J. Morasch, V. Streibel, T. Toupance, W. Jaegermann, A. Klein, The Work Function of TiO2, Surfaces 1 (1) (Sep. 2018) 73–89, https://doi.org/10.3390/surfaces1010007.

[123] M. Chen, et al., Cesium Titanium(IV) Bromide Thin Films Based Stable Lead-free Perovskite Solar Cells, Joule 2 (3) (Mar. 2018) 558–570, https://doi.org/10.1016/j.joule.2018.01.009.

[124] H. Kim, H.J. Choi, Thickness dependence of work function, ionization energy, and electron affinity of Mo and W dichalcogenides from DFT and GW calculations, Phys. Rev. B 103 (8) (Feb. 2021) 085404, https://doi.org/10.1103/PhysRevB.103.085404.

[125] H.R. Atapattu, et al., A'-Site dipole magnitude and direction dominate the ionization energy and electron affinity of layered metal-halide perovskites, J. Am. Chem. Soc. 147 (30) (Jul. 2025) 26898–26906, https://doi.org/10.1021/jacs.5c08621.

[126] I. Musa, N. Qamhieh, J. Ghabboun, S.T. Mahmoud, Investigation of tunable work function, electrostatic force microscopy and band structure of TiO2 nanoparticles using Kelvin probe force microscopy, Materials 9 (Oct. 2025) 101088, https://doi.org/10.1016/j.nxmate.2025.101088.

[127] M. Wei, C.-F. Li, X.-R. Deng, H. Deng, Surface work function of transparent conductive ZnO films, Energy Procedia 16 (2012) 76–80, https://doi.org/10.1016/j.egypro.2012.01.014.

[128] J. Xu, W. Wang, S. Sun, L. Wang, Enhancing visible-light-induced photocatalytic activity by coupling with wide-band-gap semiconductor: a case study on Bi2WO6/TiO2, 112, Appl. Catal. B 111 (Jan. 2012) 126–132, https://doi.org/10.1016/j.apcatb.2011.09.025.

[129] P. Lou, J.Y. Lee, A new crystal family of GaNGeC quaternary compounds including direct band gap semiconductors and metals, Mater, Adv 2 (2021) 3420–3425, https://doi.org/10.1039/D0MA00844C.

[130] T.-N. Do, et al., Electronic and photocatalytic properties of two-dimensional boron phosphide/SiC van der Waals heterostructure with direct type-II band alignment: a first principles study, RSC Adv. 10 (53) (2020) 32027–32033, https://doi.org/10.1039/D0RA05579D.

[131] V. Stevanović, S. Lany, D.S. Ginley, W. Tumas, A. Zunger, Assessing capability of semiconductors to split water using ionization potentials and electron affinities only, Phys. Chem. Chem. Phys. 16 (8) (2014) 3706, https://doi.org/10.1039/c3cp54589j.

[132] S. Nishioka, F.E. Osterloh, X. Wang, T.E. Mallouk, K. Maeda, Photocatalytic water splitting, Nat. Rev. Methods Prim. 3 (1) (Jun. 2023) 42, https://doi.org/10.1038/s43586-023-00226-x.

[133] Y. Rouzhahong, M. Wushuer, M. Mamat, Q. Wang, Q. Wang, First Principles Calculation for Photocatalytic Activity of GaAs Monolayer, Sci. Rep. 10 (1) (Jun. 2020) 9597, https://doi.org/10.1038/s41598-020-66575-9.

[134] H. Reshak, V.V. Atuchin, S. Auluck, I.V. Kityk, First and second harmonic generation of the optical susceptibilities for the non-centro-symmetric orthorhombic $AgCd_2GaS_4$, J. Phys. Condens. Matter 20 (32) (Aug. 2008) 325234, https://doi.org/10.1088/0953-8984/20/32/325234.

[135] L. Ma, et al., Engineering oxygen vacancies towards self-activated $BaLuAl_xZn_{4-x}O_{7-(1-x)/2}$ photoluminescent materials: an experimental and theoretical analysis, Phys. Chem. Chem. Phys. 17 (46) (2015) 31188–31194, https://doi.org/10.1039/C5CP05130D.

[136] Y. Zhuravlev, V. Atuchin, Nonlinear optical, dielectric, and piezoelectric properties of hexagonal fluorocarbonates $ABCO_3F$ (A: K, Rb, Cs; B: Mg, Ca, Sr, Zn, Cd, Pb) from first principles, J. Nonlinear Opt. Phys. Mater. 34 (05) (Aug. 2025), https://doi.org/10.1142/S0218863524500127.

[137] X. Peng, Q. Wei, A. Copple, Strain-engineered direct-indirect band gap transition and its mechanism in two-dimensional phosphorene, Phys. Rev. B 90 (8) (Aug. 2014) 085402, https://doi.org/10.1103/PhysRevB.90.085402.

[138] H. Sabbah, Z. Abdel Baki, R. Mezher, J. Arayro, SCAPS-1D modeling of hydrogenated lead-free Cs2AgBiBr6 double perovskite solar cells with a remarkable efficiency of 26.3, Nanomaterials 14 (1) (Dec. 2023) 48, https://doi.org/10.3390/nano14010048.

[139] M. Bilal, S. Jalali-Asadabadi, R. Ahmad, I. Ahmad, Electronic properties of antiperovskite materials from state-of-the-art density functional theory, J. Chem. 2015 (2015) 1–11, https://doi.org/10.1155/2015/495131.

[140] Z. Jia, et al., Applications of all-inorganic perovskites for energy storage, Mater. Adv. 4 (1) (2023) 79–104, https://doi.org/10.1039/d2ma00779g.

[141] W. Xia, et al., Antiperovskite electrolytes for solid-state batteries, Chem. Rev. 122 (3) (Feb. 2022) 3763–3819, https://doi.org/10.1021/acs.chemrev.1c00594.

[142] Md.A.B. Shanto, et al., Investigating how the electronic and optical properties of a novel cubic inorganic halide perovskite, Sr3NI3 are affected by strain, F1000Res 12 (Aug. 2023) 1005, https://doi.org/10.12688/f1000research.137044.1.

[143] S. Niu, X. Liu, C. Wang, W. Mu, W. Xu, Q. Wang, Breaking the Trade-Off between complexity and absorbing performance in metamaterials through intelligent design, Small 21 (24) (Jun. 2025), https://doi.org/10.1002/smll.202502828.

[144] Md.S. Islam, et al., Investigation strain effects on the electronic, optical, and output performance of the novel inorganic halide perovskite Sr3SbI3 solar cell, Chin. J. Phys. 88 (Apr. 2024) 270–286, https://doi.org/10.1016/j.cjph.2024.01.011.

[145] Z. Xie, L. Hui, J. Wang, G. Zhu, Z. Chen, C. Li, Electronic and optical properties of monolayer black phosphorus induced by bi-axial strain, Comput. Mater. Sci. 144 (Mar. 2018) 304–314, https://doi.org/10.1016/j.commatsci.2017.12.026.

[146] A.B. Kuzmenko, Kramers–Kronig constrained variational analysis of optical spectra, Rev. Sci. Instrum. 76 (8) (Aug. 2005), https://doi.org/10.1063/1.1979470.

[147] S. Chen, G. Xu, X. Zhang, T. Peng, Y. Sun, X. Wang, Strain-dependent work function of metal surfaces: Insights from first-principles investigation, Phys. B

Condens Matter 690 (Oct. 2024) 416288, https://doi.org/10.1016/j.physb.2024.416288.

[148] Md.E. Ali, DFT-based investigation of optoelectronic, dynamic, thermodynamic, mechanical, and strain-engineered properties of a novel lead-free Na3SBr inorganic anti-perovskite and achieving over 27% solar cell efficiency, J. Alloy. Compd. 1043 (Oct. 2025) 184221, https://doi.org/10.1016/j.jallcom.2025.184221.

[149] C.V. Ramana, et al., Spectroscopic ellipsometry characterization of the optical properties and thermal stability of ZrO2 films made by ion-beam assisted deposition, Appl. Phys. Lett. 92 (1) (Jan. 2008), https://doi.org/10.1063/1.2811955.

[150] N. Gasimov, et al., Depolarization effect in rare-earth doped Y_2O_3 films in blue and UV spectral range, Phys. Status Solidi C. 12 (6) (Jun. 2015) 600–604, https://doi.org/10.1002/pssc.201400301.

[151] V. Garg, et al., Investigation of dual-ion beam sputter-instigated plasmon generation in TCOs: a case study of GZO, ACS Appl. Mater. Interfaces 10 (6) (Feb. 2018) 5464–5474, https://doi.org/10.1021/acsami.7b15103.

[152] V.V. Atuchin, et al., Structural, spectroscopic, and electronic properties of Cubic G0-Rb_2KTiOF_5 oxyfluoride, J. Phys. Chem. C. 117 (14) (Apr. 2013) 7269–7278, https://doi.org/10.1021/jp401391y.

[153] X. Nie, Z. Yu, E. Jackson, J. Lee, Refractive index and extinction coefficient of hollow microspheres for solar reflection, Appl. Phys. Lett. 118 (21) (May 2021), https://doi.org/10.1063/5.0049018.

[154] X. Ziang, et al., Refractive index and extinction coefficient of CH_3NH_3PbI_3 studied by spectroscopic ellipsometry, Opt. Mater. Express 5 (1) (Jan. 2015) 29, https://doi.org/10.1364/OME.5.000029.

[155] C. Claeys, E. Simoen, Radiation Effects in Advanced Semiconductor Materials and Devices, 57, Springer Berlin Heidelberg, Berlin, Heidelberg, 2002, https://doi.org/10.1007/978-3-662-04974-7.

[156] J. Grum, Book review: electronic and optoelectronic properties of semiconductor structures by Jasprit Singh, Int. J. Microstruct. Mater. Prop. 4 (3) (2009) 391, https://doi.org/10.1504/IJMMP.2009.031146.

[157] Bhattacharya, Pallab, Semiconductor optoelectronic devices, 4379-31–4379, Choice Rev. Online 31 (08) (Apr. 1994) 31, https://doi.org/10.5860/CHOICE.31-4379.

[158] B.E.A. Saleh, M.C. Teich, Fundamentals of Photonics, Wiley, 1991, https://doi.org/10.1002/0471213748.

[159] X. Fu, Z. Niu, C. Peng, H. Han, W. Sun, T. Yue, Quantitative synergistic adsorption affinity of Ca(II) and sodium oleate to predict the surface reactivity of hematite and quartz, Sep Purif. Technol. 360 (Jul. 2025) 131196, https://doi.org/10.1016/j.seppur.2024.131196.

[160] J. Yu, et al., Regulating socketed geometry of nanoparticles on perovskite oxide supports for enhanced stability in oxidation reactions, Nat. Commun. 15 (1) (Nov. 2024) 10229, https://doi.org/10.1038/s41467-024-54546-x.

[161] D. Metzner, M. Olbrich, P. Lickschat, A. Horn, S. Weißmantel, Experimental and theoretical determination of the effective penetration depth of ultrafast laser radiation in stainless steel, Lasers Manuf. Mater. Process. 7 (4) (Dec. 2020) 478–495, https://doi.org/10.1007/s40516-020-00129-9.

[162] H.J. Lee, M.M.A. Gamel, P.J. Ker, M.Z. Jamaludin, Y.H. Wong, J.P.R. David, Absorption Coefficient of Bulk III-V semiconductor materials: a review on methods, properties and future prospects, J. Electron Mater. 51 (11) (Nov. 2022) 6082–6107, https://doi.org/10.1007/s11664-022-09846-7.

[163] A. Nayfeh, S. Abdul Hadi, Si1–Ge deposition and properties. Silicon-Germanium Alloys for Photovoltaic Applications, Elsevier, 2023, pp. 37–61, https://doi.org/10.1016/B978-0-323-85630-0.00003-0.

[164] M. Krimi, M. Akermi, R. Hassani, A. Ben Rhaiem, Corrigendum to 'Optical and conduction mechanism study of lead-free CsMnCl3 perovskite' [Solid State Sci. 155 (2024) 107646, Solid State Sci. 161 (Mar. 2025) 107837, https://doi.org/10.1016/j.solidstatesciences.2025.107837.

[165] M. Krimi, M. Akermi, R. Hassani, A. Ben Rhaiem, Optical and conduction mechanism study of lead-free CsMnCl3 perovskite, Solid State Sci. 155 (Sep. 2024) 107646, https://doi.org/10.1016/j.solidstatesciences.2024.107646.

[166] M. Roknuzzaman, et al., Electronic and optical properties of lead-free hybrid double perovskites for photovoltaic and optoelectronic applications, Sci. Rep. 9 (1) (Jan. 2019) 718, https://doi.org/10.1038/s41598-018-37132-2.

[167] I. Khan, A. Ullah, N. Rahman, M. Husain, V. Tirth, M. Sohail, First principle study of structural and optoelectronic properties of ZnLiX3 (X = Cl or F) perovskites, Results Phys. 66 (Nov. 2024) 108019, https://doi.org/10.1016/j.rinp.2024.108019.

[168] R.K. Pingak, et al., A DFT investigation of lead-free $TlSnX_3$ (X = Cl, Br, or I) perovskites for potential applications in solar cells and thermoelectric devices, RSC Adv. 13 (48) (2023) 33875–33886, https://doi.org/10.1039/D3RA06685A.

[169] X. Liang, Q. Ke, X. Zhao, X. Chen, Graphene-supported tin single-atom catalysts for CO_2 hydrogenation to HCOOH: a theoretical investigation of performance under different N coordination numbers, ACS Appl. Nano Mater. 6 (6) (Mar. 2023) 4489–4498, https://doi.org/10.1021/acsanm.2c05581.

[170] D. Zhang, H. Xie, S. Chen, G. Zhou, Porous CoCe composite catalyst prepared by hydrothermal assisted soft template method for CH4/CO2 dry reforming, Fuel 327 (Nov. 2022) 125105, https://doi.org/10.1016/j.fuel.2022.125105.

[171] S. Ali, et al., Cobalt coordinated two-dimensional covalent organic framework a sustainable and robust electrocatalyst for selective CO2 electrochemical conversion to formic acid, Fuel Process. Technol. 237 (Dec. 2022) 107451, https://doi.org/10.1016/j.fuproc.2022.107451.

[172] S. Ali, P.M. Ismail, M. Humayun, H. Abu-Farsakh, M. Bououdina, F. Jan, Mechanistic insights into CO2 reduction on C3N3 supported single atom catalysts: A DFT study, Mol. Catal. 586 (Nov. 2025) 115439, https://doi.org/10.1016/j.mcat.2025.115439.

[173] S. Ali, Z. Lian, B. Li, Density Functional Theory Study of a Graphdiyne-Supported Single Au Atom Catalyst for Highly Efficient Acetylene Hydrochlorination, ACS Appl. Nano Mater. 4 (6) (Jun. 2021) 6152–6159, https://doi.org/10.1021/acsanm.1c00945.

[174] S. Ali, et al., Benchmarking the two-dimensional conductive Y3(C6X6)2 (Y = Co, Cu, Pd, Pt; X = NH, NHS, S) metal-organic framework nanosheets for CO2 reduction reaction with tunable performance, Fuel Process. Technol. 236 (Nov. 2022) 107427, https://doi.org/10.1016/j.fuproc.2022.107427.

[175] O. Ahmad, et al., Modelling and numerical simulations of eco-friendly double absorber solar cell 'Spiro-OmeTAD/CIGS/MASnI3/CdS/ZnO' and its PV-module, Org. Electron 117 (Jun. 2023) 106781, https://doi.org/10.1016/j.orgel.2023.106781.

[176] S.H. Cheragee, J.A. Akhi, M. Dev, Md.M. Haque, M.J. Alam, Numerical design of non-toxic high-efficiency tandem solar cell with distinct hole transport materials, Thin Solid Films 801 (Jul. 2024) 140432, https://doi.org/10.1016/j.tsf.2024.140432.

[177] N.K. Singh, A. Agarwal, A.K. Singh, S.N. Singh, Design and performance evaluation of eco-friendly FASnI3/CsSn0.5Ge0.5I3 based perovskite solar cell with distinct charge transport layer: A computational modeling, Sol. Energy 268 (Jan. 2024) 112256, https://doi.org/10.1016/j.solener.2023.112256.

[178] E. Tinedert, A. Saadoune, M.K. Hossain, A theoretical study of all-inorganic perovskite solar cells: computational modeling of the CsPbI3/RbGeI3 bilayer absorber structure, J. Phys. Chem. Solids 189 (Jun. 2024) 111951, https://doi.org/10.1016/j.jpcs.2024.111951.

[179] M. Belarbi, O. Zeggai, S. Khettaf, S. Louhibi-Fasla, Efficiency enhancement of triple absorber layer perovskite solar cells with the best materials for electron and hole transport layers: numerical study, Semicond. Sci. Technol. 37 (9) (Sep. 2022) 095016, https://doi.org/10.1088/1361-6641/ac83e4.

[180] Y. El Arfaoui, M. Khenfouch, N. Habiballah, Efficient all lead-free perovskite solar cell simulation of FASnI3/FAGeCl3 with 30% efficiency: SCAPS-1D investigation, Results Opt. 13 (Dec. 2023) 100554, https://doi.org/10.1016/j.rio.2023.100554.

[181] S.M. Hasnain, I. Qasim, A. Iqbal, M. Amin. Mir, N. Abu-Libdeh, Novel dual absorber configuration for eco-friendly perovskite solar cells: design, numerical investigations and performance of ITO-C60-MASnI3-RbGeI3-Cu2O-Au, Sol. Energy 278 (Aug. 2024) 112788, https://doi.org/10.1016/j.solener.2024.112788.

[182] S. Bhattarai, et al., Perovskite solar cells with dual light absorber layers for performance efficiency exceeding 30, Energy Fuels 37 (14) (Jul. 2023) 10631–10641, https://doi.org/10.1021/acs.energyfuels.3c01659.

[183] M. Robayet Bakhtear Thoha, Md.M. Haque, Md.E. Ali, Modeling of a novel CuAgBeSnSe4/FASnI3-based perovskite solar cell with optimized device parameters, Results Eng. (Nov. 2025) 108103, https://doi.org/10.1016/j.rineng.2025.108103.

[184] M.Y. Chern, D.A. Vennos, F.J. Disalvo, Synthesis, structure, and properties of anti-perovskite nitrides Ca3MN, M=P, As, Sb, Bi, Ge, Sn, and Pb, J. Solid State Chem. 96 (2) (Feb. 1992) 415–425, https://doi.org/10.1016/S0022-4596(05)80276-2.

[185] E. Ahiavi, et al., Mechanochemical synthesis and ion transport properties of Na3OX (X = Cl, Br, I and BH4) antiperovskite solid electrolytes, J. Power Sources 471 (Sep. 2020) 228489, https://doi.org/10.1016/j.jpowsour.2020.228489.

[186] P. Hoffmann, D.I. Villalva-Mejorada, O.W. Elkhafif, T. Diemant, T. Jacob, H. K. Hassan, Is Mg_3AsN antiperovskite a promising Mg-ion conductor? Mater. Horiz. (2025) https://doi.org/10.1039/D5MH01361E.

[187] A. Husainat, W. Ali, P. Cofie, J. Attia, J. Fuller, Simulation and Analysis of Methylammonium Lead Iodide (CH₃NH₃PbI₃) Perovskite Solar Cell with Au Contact Using SCAPS 1D Simulator, Am. J. Opt. Photonics 7 (2) (2019) 33, https://doi.org/10.11648/j.ajop.20190702.12.

[188] M. Faghihnasiri, M. Izadifard, M.E. Ghazi, DFt study of mechanical properties and stability of cubic methylammonium lead halide perovskites ($CH_3NH_3PbX_3$, X = I, Br, Cl), J. Phys. Chem. C. 121 (48) (Dec. 2017) 27059–27070, https://doi.org/10.1021/acs.jpcc.7b07129.

[189] A.M.A. Leguy, et al., Dynamic disorder, phonon lifetimes, and the assignment of modes to the vibrational spectra of methylammonium lead halide perovskites, Phys. Chem. Chem. Phys. 18 (39) (2016) 27051–27066, https://doi.org/10.1039/C6CP03474H.

[190] A. ul Rehman, et al., Performance optimization of FASnI3 based perovskite solar cell through SCAPS-1D simulation, Hybrid. Adv. 7 (Dec. 2024) 100301, https://doi.org/10.1016/j.hybadv.2024.100301.

[191] S. Pachori, R. Agrawal, A. Shukla, A. Singh Verma, First-principles calculations for fundamental and spectroscopic screening of hybrid perovskite (HC(NH2) 2PbI3) formamidinium lead iodide, Mater. Chem. Phys. 287 (Aug. 2022) 126149, https://doi.org/10.1016/j.matchemphys.2022.126149.

[192] L. Guo, G. Tang, J. Hong, Mechanical properties of formamidinium halide perovskites $FABX_3$ (FA=CH(NH$_2$ $_2$; B=Pb, Sn; X=Br, I) by first-principles calculations *, Chin. Phys. Lett. 36 (5) (May 2019) 056201, https://doi.org/10.1088/0256-307X/36/5/056201.

[193] M.I. Amanyi, et al., SCAPS-1D analysis of non-toxic lead-free MASnI3 perovskite-based solar cell using inorganic charge transport layers, East Eur. J. Phys. (3) (Sep. 2024) 447–455, https://doi.org/10.26565/2312-4334-2024-3-54.

[194] I.O.A. Ali, D.P. Joubert, M.S.H. Suleiman, First-principles study of structural, mechanical, dynamical stability, electronic and optical properties of orthorhombic CH3NH3SnI3 under pressure, Eur. Phys. J. B 92 (9) (Sep. 2019) 202, https://doi.org/10.1140/epjb/e2019-100101-1.